



Research article

Non-local multiscale approach for the impact of go or grow hypothesis on tumour-viruses interactions

Abdulhamed Alsis¹, Raluca Eftimie² and Dumitru Trucu^{1,*}

¹ Division of Mathematics, University of Dundee, Dundee DD1 4HN, United Kingdom

² Laboratoire Mathématiques de Besançon, UMR-CNRS 6623, Université de Bourgogne Franche-Comté, 16 Route de Gray, Besançon, France

* **Correspondence:** Email: trucu@maths.dundee.ac.uk

Abstract: We propose and study computationally a novel non-local multiscale moving boundary mathematical model for tumour and oncolytic virus (OV) interactions when we consider the *go or grow* hypothesis for cancer dynamics. This spatio-temporal model focuses on two cancer cell phenotypes that can be infected with the OV or remain uninfected, and which can either move in response to the extracellular-matrix (ECM) density or proliferate. The interactions between cancer cells, those among cancer cells and ECM, and those among cells and OV occur at the macroscale. At the micro-scale, we focus on the interactions between cells and matrix degrading enzymes (MDEs) that impact the movement of tumour boundary. With the help of this multiscale model we explore the impact on tumour invasion patterns of two different assumptions that we consider in regard to cell-cell and cell-matrix interactions. In particular we investigate model dynamics when we assume that cancer cell fluxes are the result of local advection in response to the density of extracellular matrix (ECM), or of non-local advection in response to cell-ECM adhesion. We also investigate the role of the transition rates between mainly-moving and mainly-growing cancer cell sub-populations, as well as the role of virus infection rate and virus replication rate on the overall tumour dynamics.

Keywords: multiscale cancer modelling; non-local cell adhesion; tumour-oncolytic viruses interactions; *go or grow* hypothesis; migration-proliferation dichotomy

1. Introduction

The *go or grow* (GOG) hypothesis or the migration-proliferation dichotomy, proposes that cell proliferation and cell migration are two temporally exclusive events: cells either migrate or proliferate and they can periodically switch between proliferative and migratory states [1]. Studies on the GOG hypothesis are conflicting, with some studies supporting and confirming this hypothesis *in vitro* for

different cancer cell types (e.g., glioma, melanoma, or breast cancer) [2–9] and other studies challenging this hypothesis [1, 10, 11]. For example, Tektonidis et al. [9] presented a computational data-driven study of *in vitro* glioma invasion based on three experimental papers, and concluded that the GOG mechanism combined with self-repulsion and a density-dependent phenotypic switch is mandatory to duplicate the experimental results [7, 12]. On the other hand, Corcoran et al. [1] used time-lapse video-microscopy to monitor directional migration, invasion and mitosis of cancer cells, and concluded that in medulloblastoma cell lines there is no evidence to support the GOG hypothesis. More precisely, their results suggested that migrating and non-migrating cell lines have similar mitotic activities. Similarly, Garay et al. [10] tested this hypothesis on 12 mesothelioma, 13 melanoma and 10 lung cancer cell lines using time-lapse video-microscopy, and their results also contradicted the concept of GOG hypothesis.

Over the last decades, mathematical models have been used in addition to experimental studies to shed some light on this *go or grow* hypothesis. Many of these models are discrete models of cellular automata (CA) type or lattice gas cellular automata (LGCA) type [7, 13–17]. There are also various continuum models described by partial differential equations [11, 18–25]. These continuum models can either model separately the migrating and proliferative cancer cell sub-populations [20–22, 24], or can model them via a single equation for one cancer population that can move for some time instances and proliferate for other time instances [11, 18]. Those models that consider separate sub-populations of migrating and proliferative cancer cells incorporate also transition (i.e., switching) rates between these two sub-populations. These transition rates can be either constant [20, 26] or density dependent: they can depend for example on the total density of cells [20, 22], on the concentration of integrins bound to extracellular matrix (ECM) fibres [23], on the density of ECM fibres [25], on the level of oxygen [19, 24].

It should be mentioned here that some GOG models have been reduced to simpler forms; for example, in [20] the authors assumed that proliferating cell sub-population could stop proliferating and thus their *go-or-growth* model was reduced to a *go-or-rest* model.

The majority of continuum mathematical models in the literature for the GOG hypothesis focus mainly on local interactions between cells. However, it is known that cells can mechanically sense and react to the presence of other cells up to $100\mu\text{m}$ away [27], and thus more and more mathematical models have been recently developed to consider such non-local cell-cell and cell-ECM interactions [28–31]. Nevertheless, these nonlocal models do not usually incorporate the GOG hypothesis.

In this study we plan to investigate (for the first time – to our knowledge) the impact of the GOG hypothesis on oncolytic virotherapies. These oncolytic virotherapies are cancer therapies that use oncolytic viruses (OVs), i.e., viruses that replicate inside and destroy cancer cells. Despite some clinical successes with these oncolytic virotherapies (currently a few such viruses are in the late stages of various clinical trials [32]) there are still many open questions related to the interactions between oncolytic viruses and tumour cells [33]. And, to our knowledge, it is not clear at this moment how the spread of oncolytic viruses through the solid tumours is affected by the GOG hypothesis. In this study, we investigate this particular aspect using a modelling and computational approach, which allows us to test numerically various hypotheses related to cancer-OV interactions.

To this end, we extend our previous non-local multi-scale mathematical model for cancer-oncolytic viruses (OV) interactions [34], by considering also the GOG hypothesis. We

consider distinct proliferative and migrating cancer cell subpopulations, and assume that they can become infected with an oncolytic virus (see Figure 1). With the help of this new model, we explore numerically different aspects of the GOG hypothesis, as well as the possibility of having local vs. non-local cell interactions and their impact on cancer invasion in the context of oncolytic virotherapies. We need to emphasise here that with the help of this new model we investigate (for the first time – to our knowledge) the impact of the GOG hypothesis on oncolytic virotherapies.

We describe the new multiscale model in Section 2. The computational approach used to simulate numerically this model is described briefly in Section 3. Then, numerical simulations are presented in Section 4. We conclude in Section 5 with a brief summary and discussion of the results.

2. Mathematical model

Adopting the multiscale moving boundary modelling approach introduced initially in [35], in the following we explore the dynamic interaction between an invading heterotypic tumour and an oncolytic virus. Indeed, considering here the *go or grow* hypothesis [1], the invading tumour is assumed to consist of two subpopulations of cancer cells, namely migrating and proliferative, which exercise their dynamics within the surrounding ECM and that can become infected by an oncolytic virus over a time interval $[0, T]$. For $t \in [0, T]$, denoting by $\Omega(t)$ the spatial support of the progressing tumour that evolves inside a maximal tissue cube Y (i.e., $\Omega(t) \subset Y$), for any $x \in \Omega(t)$, let $c_m(x, t)$, $c_p(x, t)$, and $e(x, t)$ represent the spatial densities of the migrating cancer cells subpopulation, the proliferating cancer cells subpopulation, and the ECM, respectively. Furthermore, denoting here the oncolytic virus density by $v(x, t)$, $\forall x \in \Omega(t)$, as both the migrating and the proliferating cancer cells can become infected by the oncolytic virus $v(x, t)$, let $i_m(x, t)$ and $i_p(x, t)$ represent the densities of infected migrating cancer cells and proliferating cancer cells, respectively (see Figure 1).

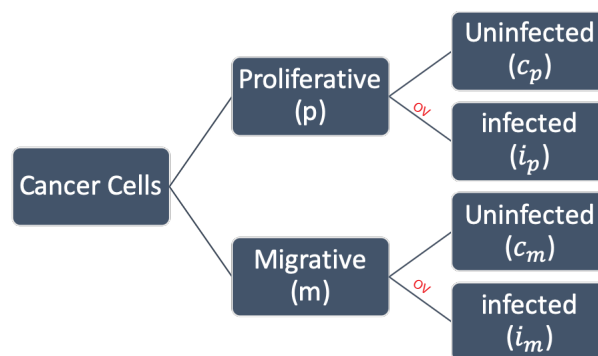


Figure 1. Schematic diagram illustrating the splitting of the overall cancer cells population into the migrating and proliferative subpopulations (according to GOG hypothesis), with each of these subpopulations further branching into corresponding infected and uninfected sub-subpopulations.

By incorporating here the GOG hypothesis, we expand and generalise the modelling framework for tumour-OV interaction proposed in [29, 34]. Indeed, building on the multiscale framework introduced in [35], we explore these complex cancer-OV interactions by accounting for the interlinked two-scale dynamics that connects the tissue-scale (macro-scale) tumour macro-dynamics with the cell-scale (micro-scale) proteolytic activity of MDEs that occurs along the invasive edge of the tumour. In the following we describe in detail the macro-dynamics, the micro-dynamics, as well as the double feed-back loop that connects the two scales of activity in our new model.

2.1. Tumour–OV interacting macro-dynamics

For each $t \in [0, t]$, and each $x \in \Omega(t)$, denoting the *total cancer cell population* by $c_{\text{total}}(x, t)$

$$c_{\text{total}}(x, t) = c_p(x, t) + i_p(x, t) + c_m(x, t) + i_m(x, t), \quad (2.1)$$

and defining the *total tumour vector* to be $\mathbf{u}(x, t) = (c_p(x, t), i_p(x, t), c_m(x, t), i_m(x, t), e(x, t))^T$, the volume fraction of space occupied by the tumour can therefore be expressed mathematically as

$$\rho(\mathbf{u}) = v_e e(x, t) + v_c (c_{\text{total}}(x, t)), \quad (2.2)$$

where v_e represents the fraction of physical space occupied by the ECM and v_c is the fraction of physical space occupied collectively by all cancer subpopulations.

For the tumour dynamics, we assume that the motility of each of the cancer cells subpopulations is due to a combination of random movement (described by linear diffusion term) and a directed migration due to cell-cell and cell-ECM adhesion. The spatial fluxes triggered by cell adhesion that cause the directed cells migration are considered here both from a local and non-local perspective [36–41], and in following we will detail their mathematical formulation. For convenience, for each cancer cell subpopulation $c \in \{c_p, c_m, i_p, i_m\}$, we consider a global notation $\varphi_c(\mathbf{u})$ describing the effect of the cell adhesion processes either locally, through adhesive interactions between cancer cells and ECM (whereby the tumour cells exercise haptotactic movement [42] towards higher levels of ECM), or non-locally, where both cell-cell and cell-ECM adhesive interactions are accounted for within an appropriate cell sensing region. Thus, $\varphi_c(\mathbf{u})$ is mathematically formalised as

$$\varphi_c(\mathbf{u}) := \begin{cases} \eta_c \nabla \cdot (c \nabla e), & \text{local haptotactic interactions between cancer cells and ECM,} \\ \nabla \cdot (c \mathcal{A}_c(\cdot, \cdot, \mathbf{u}(\cdot, \cdot))), & \text{non-local cell–cells and cell–ECM interactions on a cell sensing region,} \end{cases} \quad (2.3)$$

where, for any given subpopulation $c \in \{c_p, c_m, i_p, i_m\}$, we have that $\eta_c > 0$ is a constant haptotactic rate associated to c , while $\mathcal{A}_c(x, t, \mathbf{u}(\cdot, t))$ is a non-local spatial flux term that is detailed as follows. Indeed, following a similar approach as in [28, 43, 44], $\forall c \in \{c_p, c_m, i_p, i_m\}$, at each spatio-temporal point (x, t) the cell adhesion flux $\mathcal{A}_c(x, t, \mathbf{u}(\cdot, t))$ cumulates the strengths of the cell-cell and cell-matrix adhesion junctions that cells from cancer subpopulation c that distributed at (x, t) establish with the other cell subpopulations and the ECM distributed within an appropriate maximal sensing region $\mathbf{B}(x, R)$ of radius $R > 0$. This is formulated mathematically as

$$\mathcal{A}_c(x, t, \mathbf{u}(\cdot, t)) = \frac{1}{R} \int_{\mathbf{B}(0, R)} \mathbf{n}(y) \mathbf{K}(\|y\|_2) [S_{cc} c(x+y, t) dy + S_{ce} e(x+y, t)] (1 - \rho(\mathbf{u}))^+ \chi_{\Omega(t)}(x+y, t) dy. \quad (2.4)$$

here, $\chi_{\Omega(t)}(\cdot)$ is the characteristic function of $\Omega(t)$, while the term $(1 - \rho(\mathbf{u}))^+ := \max\{(1 - \rho(\mathbf{u})), 0\}$ enables the avoidance of local overcrowding. Further, for any $y \in \mathbf{B}(0, R)$, $\mathbf{n}(y)$ denotes the unit radial vector originating from x and pointing to $x + y \in \mathbf{B}(x, R)$, which is given by

$$\mathbf{n}(y) := \begin{cases} \frac{y}{\|y\|_2} & \text{if } y \in \mathbf{B}(0, R) \setminus \{(0, 0)\}, \\ (0, 0) & \text{otherwise.} \end{cases} \quad (2.5)$$

with $\|\cdot\|_2$ being the usual Euclidean norm. Moreover, $\mathbf{K}(\cdot) : [0, R] \rightarrow [0, 1]$ is a radially symmetric kernel that explores the dependance of the strengths of the established cell adhesion junctions on the radial distance from the centre of the sensing region x to $\zeta \in \mathbf{B}(x, R)$. Since these adhesion junction strengths are assumed to decrease as the distance $r := \|x - \zeta\|_2$ increases, \mathbf{K} therefore is taken here of the form

$$\mathbf{K}(r) := \frac{3}{2\pi R^2} \left(1 - \frac{r}{2R}\right), \quad \forall r \in [0, R]. \quad (2.6)$$

Furthermore, since in this study we focus only on self-adhesion and we do not consider cross-adhesion bonds between four cancer cells subpopulation, in Eq (2.4) we have that S_{cc} and S_{ce} for any given cancer cell subpopulation $c \in \{c_p, c_m, i_p, i_m\}$ represent the adhesive interaction strengths for the *self*-cell-cell adhesion and cell-ECM, respectively. While the cell-ECM adhesion strength S_{ce} is considered to be a positive constant, the cell-cell adhesion strength S_{cc} explores here the fact that the ability of the cell distributed at x to establish cell-cell adhesive junctions with the cells distributed at the other locations $y \in \mathbf{B}(x, R)$ depends on the amount of intercellular Ca^{2+} ions available within the ECM [45, 46]. As a consequence, adopting a similar approach to the one in [47], we assume here that S_{cc} is dependent on the ECM density and it takes the form

$$S_{cc}(e) = S_{cc}^{\max} \exp\left(1 - \frac{1}{1 - (1 - e(x, t))^2}\right), \quad (2.7)$$

with S_{cc}^{\max} representing the maximum strength of cell-cell adhesive junctions established by the cancer cells subpopulation $c \in \{c_p, c_m, i_p, i_m\}$. Therefore, the adhesive strengths for cell-cell and cell-ECM adhesion for all four cancer subpopulation can be compactly expressed via the diagonal matrices

$$\mathbf{S}_{\text{cell-cell}} = \begin{bmatrix} S_{c_p c_p} & 0 & 0 & 0 \\ 0 & S_{i_p i_p} & 0 & 0 \\ 0 & 0 & S_{c_m c_m} & 0 \\ 0 & 0 & 0 & S_{i_m i_m} \end{bmatrix} \quad \text{and} \quad \mathbf{S}_{\text{cell-ECM}} = \begin{bmatrix} S_{c_p e} & 0 & 0 & 0 \\ 0 & S_{i_p e} & 0 & 0 \\ 0 & 0 & S_{c_m e} & 0 \\ 0 & 0 & 0 & S_{i_m e} \end{bmatrix}, \quad (2.8)$$

respectively.

Finally, in the context of the GOG hypothesis, another important aspect that occurs during the tumour dynamics is the transitions between from the proliferative cancer subpopulation and the migrating one. Adopting a similar form to the one proposed in [15, 16, 26], the transition from proliferative to migrating cancer cells is captured here through the switching term λ_{c_p, c_m} that is given by

$$\lambda_{c_p, c_m} = \omega_2 c_m - \omega_1 c_p, \quad (2.9)$$

where ω_1 is the rate of switching from proliferative state c_p to migration state c_m , and ω_2 is the rate of switching from migration to proliferative state. On the other hand, the transition from migrating to

proliferative cancer cells is expressed through the switching term λ_{c_m, c_p} defined as

$$\lambda_{c_m, c_p} = -\lambda_{c_p, c_m}. \quad (2.10)$$

Thus, for each of the cancer cells subpopulation $c \in \{c_p, c_m, i_p, i_m\}$, the spatial transport is a combination of random movement (expressed through diffusion) and directed movement due adhesion (explored either locally or non-locally, and represented compactly through $\varphi_c(\mathbf{u})$). Furthermore, for the particular case of the migrating and proliferative cells subpopulation c_p , and c_m , besides the spatial transport and in addition to their own proliferation (considered here of logistic type [48, 49]), their dynamics is also affected by the cell population “exchanges” due to *proliferative-migrating transitions* (i.e., transitions between proliferative and migrating subpopulations) as well as by the presence of the oncolytic virus that is able to infect cells from both populations. Finally, for their part, the infected cancer cells subpopulations, while exercising a spatial transport of the type described above, they contribute to virus replication and die. Therefore, the dynamics for each cancer cell population can be expressed mathematically as follows.

First, the governing equation for the uninfected proliferative cancer cell subpopulation is given by

$$\frac{\partial c_p}{\partial t} = D_{c_p} \Delta c_p - \varphi_{c_p}(\mathbf{u}) + \mu_p c_p (1 - \rho(\mathbf{u})) - \varrho_p c_p v + \lambda_{c_p, c_m}, \quad (2.11)$$

where $D_{c_p} > 0$ is a constant diffusion coefficient, the term $\varphi_{c_p}(\mathbf{u})$ represents the directed movement triggered by cell-adhesion processes that corresponds to c_p and is described in Eq (2.3) for $c = c_p$. Further, $\mu_p > 0$ is an intrinsic constant proliferation rate, $\varrho_p > 0$ is the rate at which the oncolytic virus infects the proliferative cancer cell population, and λ_{c_p, c_m} is the switching term given in (2.9), representing the process through which migrating cancer cells transition towards proliferative state during the tumour dynamics.

The infected proliferative cancer cell population, $i_p(t, x)$, which emerges within this dynamics due to the OV infection of c_p , also exercises a spatio-temporal dynamics that is governed by the following equation

$$\frac{\partial i_p}{\partial t} = D_{i_p} \Delta i_p - \varphi_{i_p}(\mathbf{u}) + \varrho_p c_p v - \delta_{i_p} i_p, \quad (2.12)$$

where $D_{i_p} > 0$ is a constant random motility coefficient, and $\varphi_{i_p}(\mathbf{u})$ is the spatial influence of the cell-adhesion processes that is described in Eq (2.3) and corresponds to i_p . The cancer cell population increases with at rate ϱ_p due to the new infections of the proliferative cancer cells, and decreases at rate $\delta_{i_p} > 0$ due to infected cell death.

Further, since for the migrating cancer cell population we always take into account not only cell-ECM adhesion but also cell-cell self-adhesion, the directed cell migration term $\varphi_{c_m}(\mathbf{u})$ that is defined in Eq (2.3) and corresponds to c_m is in this case constantly of the non-local form

$$\varphi_{c_m}(\mathbf{u}) = \nabla \cdot (c_m \mathcal{A}_{c_m}(\cdot, \cdot, \mathbf{u}(\cdot, \cdot))),$$

where the spatial flux $\mathcal{A}_{c_m}(\cdot, \cdot, \mathbf{u}(\cdot, \cdot))$ is the one defined in Eq (2.4) for $c = c_m$. As a consequence, the governing equation for the uninfected migrating cell population is

$$\frac{\partial c_m}{\partial t} = D_{c_m} \Delta c_m - \nabla \cdot (c_m \mathcal{A}_{c_m}) + \mu_m c_m (1 - \rho(\mathbf{u})) - \varrho_m c_m v + \lambda_{c_m, c_p}, \quad (2.13)$$

where $D_{c_m} > 0$ is a constant diffusion coefficient, $\mu_m > 0$ is a constant proliferation coefficient, $\varrho_m > 0$ is a constant rate at which the uninfected migrating population diminishes due to infection by the oncolytic virus v . Further, λ_{c_m, c_p} is the switching term given in Eq (2.10) that represents the net transition from the proliferative into the uninfected migrating state that occurs per unit time during the tumour dynamics.

The fourth tumour cell population is the infected migrating cancer cell subpopulation $i_m(t, x)$ that emerges within this dynamics due to infections by the OV, and its spatio-temporal dynamics is governed by the following equation

$$\frac{\partial i_m}{\partial t} = D_{i_m} \Delta i_m - \varphi_{i_p}(\mathbf{u}) + \varrho_m c_m v - \delta_{i_m} i_m. \quad (2.14)$$

where $D_{i_m} > 0$ is a constant random motility coefficient, and $\varphi_{i_m}(\mathbf{u})$ represents the directed migration induced by the cell-adhesion processes that corresponds to i_m and is described in Eq (2.3) for $c = i_m$. Further, the infected migrating population expand at a rate ϱ_m due to new infections occurring among the uninfected migrating cells, and they also die at rate $\delta_{i_m} > 0$.

At the same time, the ECM is degraded by both uninfected and infected cancer cell populations and is remodelled within the limit of available space. Thus, its governing dynamics is given mathematically by

$$\frac{\partial e}{\partial t} = -e(\alpha_{c_p} c_p + \alpha_{i_p} i_p + \alpha_{c_m} c_m + \alpha_{i_m} i_m) + \mu_2 e(1 - \rho(\mathbf{u})), \quad (2.15)$$

where $\alpha_{c_p} > 0$, $\alpha_{i_p} > 0$, $\alpha_{c_m} > 0$, and $\alpha_{i_m} > 0$ are the ECM degradation rates caused by cancer cells subpopulation c_p , i_p , c_m , and i_m , respectively. Further, $\mu_2 > 0$ is a constant ECM remodelling rate.

Concerning the oncolytic virus spatio-temporal dynamics, we adopt here a similar reasoning as in [34], and we assume that the OV motion is described by a random movement that is biased by a "haptotactic-like" spatial transport towards higher ECM levels. Thus, the dynamics of the oncolytic virus that we consider here is governed by

$$\frac{\partial v}{\partial t} = D_v \Delta v - \eta_v \nabla \cdot (v \nabla e) + b_m i_m + b_p i_p - (\varrho_m c_m + \varrho_p c_p) v - \delta_v v, \quad (2.16)$$

where $D_v > 0$ is a constant random motility coefficient, $\eta_v > 0$ is a constant haptotactic coefficient, $b_m, b_p > 0$ are a viral replication rates within infected proliferating and infected migrating cancer cells, respectively, and $\delta_v > 0$ is the viral decay rate.

Finally, the coupled interacting tumour – OV macro-dynamics is governed by Eqs (2.11)–(2.16) in the presence of initial conditions

$$c_p(x, 0) = c_p^0(x), \quad i_p(x, 0) = i_p^0(x), \quad c_m(x, 0) = c_m^0(x), \quad \text{and} \quad i_m(x, 0) = i_m^0(x), \quad \forall x \in \Omega(0), \quad (2.17)$$

while assuming zero-flux boundary conditions at the moving tumour interface $\partial\Omega(t)$.

2.2. Micro-scale dynamics

During their macro-scale dynamics, the four cancer cells subpopulations that get near the tumour interface (i.e., within the outer proliferating rim of the tumour) are able to secrete matrix degrading enzymes (such as the matrix metalloproteinases [50, 51]), providing this way a source of MDEs for a cell-scale (micro-scale) proteolytic micro-dynamics that takes place along the invasive edge of the tumour. Indeed, in the presence of this source of MDEs (induced by the tumour macro-dynamics), a cross-interface micro-scale MDEs spatial transport occurs within a micro-scale neighbourhood of the

tumour boundary of an appropriate cell-scale thickness $\epsilon > 0$, denoted here simply by $\mathcal{N}_\epsilon(\partial\Omega(t))$. The areas of significant ECM degradation caused by the pattern of propagation of the advancing front of MDEs within the peritumoural region $\mathcal{N}_\epsilon(\partial\Omega(t)) \setminus \Omega(t)$ will ultimately be explored by the cancer cells that will progress in those regions [51], and so precisely these boundary regions (affected by significant ECM degradation) will shape the pattern of tumour progression. Thus, following the modelling approach introduced in [35] we depict these regions of significant ECM degradations by exploring the MDEs micro-dynamic processes within $\mathcal{N}_\epsilon(\partial\Omega(t))$, which enables us ultimately to determine the law of the macro-scale tumour boundary movement.

To formalise these laws of macro-scale boundary movement induced by the boundary MDEs micro-dynamics, we adopt here the approach introduced in [35]. Therefore, the micro-scale neighbourhood $\mathcal{N}_\epsilon(\partial\Omega(t))$ is given here as a union of a covering bundle of ϵ – size overlapping micro-domains $\{\epsilon Y\}_{\epsilon Y \in \mathcal{P}_\epsilon(t)}$, namely,

$$\mathcal{N}_\epsilon(\partial\Omega(t)) := \bigcup_{\epsilon Y \in \mathcal{P}_\epsilon(t)} \epsilon Y.$$

This enables us to decompose the MDEs micro-dynamics on $\mathcal{N}_\epsilon(\partial\Omega(t))$ by exploring this as a union of micro-dynamic processes occurring on each $\epsilon Y \in \mathcal{P}_\epsilon(t)$. At any instance in time $t_0 > 0$, on each micro-domain $\epsilon Y \in \mathcal{P}_\epsilon(t_0)$, a source of MDEs appears at every micro-scale location $z \in \epsilon Y \cap \Omega(t_0)$ as a collective contribution of all the cells (both infected and uninfected) from the tumour outer proliferating rim that arrive during their dynamics within a distance $\rho > 0$ from z . Thus, over any small time interval of length $\Delta t > 0$, $[t_0, t_0 + \Delta t]$ and at any micro-scale spatial location $z \in \epsilon Y$, this MDEs source is therefore given as

$$f_{\epsilon Y}(z, \tau) = \begin{cases} \frac{\int_{\mathbf{B}(z, \rho) \cap \Omega(t_0)} (\gamma_{c_p} c_p + \gamma_{i_p} i_p + \gamma_{c_m} c_m + \gamma_{i_m} i_m)(x, t_0 + \tau) dx}{\lambda(\mathbf{B}(z, \rho) \cap \Omega(t_0))}, & z \in \epsilon Y \cap \Omega(t_0), \\ 0, & \text{otherwise,} \end{cases} \quad (2.18)$$

where $\lambda(\cdot)$ is the standard Lebesgue measure on \mathbb{R}^N , the ball $\mathbf{B}(z, r) := \{x \in Y : \|z - x\|_\infty \leq r\}$ is the maximal outer proliferating rim region from where cells that get to contribute to the formation of MDEs source at $(z, \tau) \in \epsilon Y \times [t_0, t_0 + \Delta t]$, and γ_{c_p} , γ_{i_p} , γ_{c_m} , γ_{i_m} are all positive constants representing the contributions of the cancer subpopulations of uninfected proliferative cells, infected cancer cells, uninfected migrating cells, and infected migrating cells, respectively.

In the presence of the micro-scale source of MDEs induced from the macro-dynamics on each micro-domain ϵY , these matrix degrading enzymes exhibits a diffusion transport process within the entire ϵY . Thus, denoting the MDEs distribution at $(z, \tau) \in \epsilon Y \times [0, \Delta t]$ by $m(z, \tau)$, the MDEs micro-dynamics on each ϵY is given by

$$\frac{\partial m}{\partial \tau} = D_m \Delta m + f_{\epsilon Y}(z, \tau) \quad (2.19)$$

where $z \in \epsilon Y$, $\tau \in [0, \Delta t]$. Furthermore, since we assume no pre-existing MDEs within ϵY prior to the initiation of the proteolytic micro-dynamics, the MDEs micro-dynamics Eq (2.25g) takes place in the presence of zero initial conditions. Furthermore, we assume the presence of zero-flux boundary condition, namely

$$\begin{aligned} m(z, 0) &= 0, \\ \mathbf{n} \cdot \nabla m|_{\partial\Omega} &= 0, \end{aligned} \quad (2.20)$$

where $\mathbf{n}_{\epsilon Y}$ is the outward unit normal on the frontier of the micro-domain $\partial\epsilon Y$.

2.3. Bottom-up feedback: the macro-scale tumour boundary movement induced by the boundary MDEs micro-dynamics

During the micro-dynamics Eqs (2.19) and (2.20), the MDEs transported across the interface in the peritumoural region $\epsilon Y \setminus \Omega(t_0)$ interact with ECM distribution that they encounter, resulting in degradation of ECM constituents. The advancement of MDEs within the peritumoural region $\epsilon Y \setminus \Omega(t)$ lead to a degradation of the ECM in that cell-scale region, and determines the way the macroscopic tumour boundary evolves, leading to the establishment of a boundary movement law. Indeed, following the derivation in [35], the MDEs micro-dynamics on each micro-domain ϵY enables us to derive the movement characteristics for the relocation of the macro-scale tumour boundary $\partial\Omega(t) \cap \epsilon Y$, expressing these through the derivation of a direction of movement $\eta_{\epsilon Y}$ and a displacement magnitude $\xi_{\epsilon Y}$ in that direction for the advancement of $\partial\Omega(t) \cap \epsilon Y$ within the peritumoural region $\mathcal{N}_\epsilon(\partial\Omega(t)) \setminus \Omega(t)$. To simplify the representation, the choreographic movement exercised by the $\partial\Omega(t) \cap \epsilon Y$ over a given time span $[t_0, t_0 + \Delta t]$ is represented back at macro-scale through the movement of the associated boundary midpoint $x_{\epsilon Y}^*$ of ϵY (defined topologically with full details in [35], and which can be regarded as “the center of $\partial\Omega(t) \cap \epsilon Y$ ”), as illustrated in Figure 2. For completeness, we briefly outline below the main steps involved in deriving the boundary relocation characteristics that were introduced in [35].

On the cell-scale neighbouring bundle $\mathcal{N}_\epsilon(\partial\Omega(t_0))$ of the tumour interface, for each of the boundary micro-domains $\epsilon Y \in \mathcal{P}(t_0)$ at a given a time instance $t_0 > 0$, we use the regularity property of Lebesgue measure [52] to depict the first dyadic decomposition $\{\mathcal{D}_k\}_{k \in I_{\epsilon Y}}$ of ϵY that has the property that the union of those dyadic cubes \mathcal{D}_k included in the complement of $\Omega(t_0)$ approximate to a given global micro-scale accuracy $\delta_{\Omega(t_0)} > 0$. This is schematically illustrated by the small green squares in Figure 2 that are situated outside the black tumour boundary $\partial\Omega(t_0) \cap \epsilon Y$. Further, denoting by y_k the barycenter of \mathcal{D}_k , we sub-select a sub-family of dyadic cubes $\{\mathcal{D}_k\}_{k \in I_{\epsilon Y}^*} \subset \{\mathcal{D}_k\}_{k \in I_{\epsilon Y}}$ that consists only of those dyadic cubes that are situated furthest away from the boundary midpoint $x_{\epsilon Y}^*$ (corresponding to ϵY) with the property that they carry an amount of MDEs above the mean of MDEs transported within the entire peritumoural region $\epsilon Y \setminus \Omega(t_0)$, hence covering precisely the region of significant ECM degradation caused by MDEs within $\epsilon Y \setminus \Omega(t_0)$, as illustrated in Figure 2. Thus, by cumulating the contribution to the significant ECM degradation within $\epsilon Y \setminus \Omega(t_0)$ of all the dyadic cubes $\{\mathcal{D}_k\}_{k \in I_{\epsilon Y}^*}$ while accounting on both their relative spatial location with respect to $x_{\epsilon Y}^*$ and the amount of MDEs that they get to carry at time $\tau_f := t_0 + \Delta t$, we obtain the direction of choreographic boundary relocation (exercised by the $\partial\Omega(t) \cap \epsilon Y$) due to micro-scale MDEs degradation. Therefore, this boundary movement direction is given by the positive direction of the emerging line defined by the position vectors involved $\{\overrightarrow{y_k x_{\epsilon Y}^*}\}_{k \in I_{\epsilon Y}^*}$ magnified accordingly by the MDEs mass that each dyadic cube in $\{\mathcal{D}_k\}_{k \in I_{\epsilon Y}^*}$, carries, namely

$$\eta_{\epsilon Y} = x_{\epsilon Y}^* + \nu \sum_{k \in I_{\epsilon Y}^*} \left(\int_{\mathcal{D}_k} m(z, \tau_f) dz \right) (y_k - x_{\epsilon Y}^*), \quad \nu \in [0, \infty). \quad (2.21)$$

Furthermore, the magnitude of the actual boundary movement in direction $\eta_{\epsilon Y}$ is appropriately given as a weighted sum of the Euclidean magnitudes of the position vectors $\{\|y_k x_{\epsilon Y}^*\|_2\}_{k \in I_{\epsilon Y}^*}$, with the weights

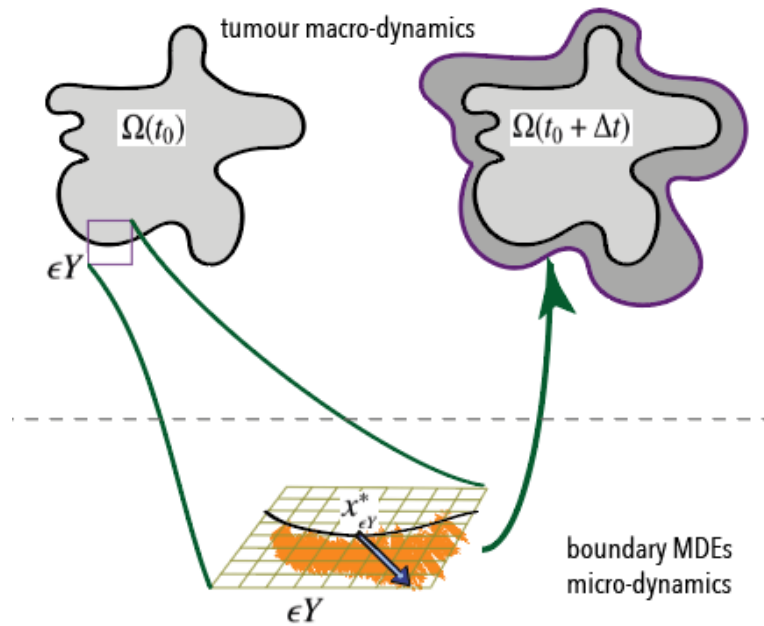


Figure 2. Illustration of the two-scale dynamics with the links between the tumour macro-dynamics and the boundary MDEs micro-dynamics that triggers the macro-scale cancer boundary movement. In orange we have the peritumoural region of significant degradation of ECM caused by the MDEs transported on $\epsilon Y \setminus \Omega(t_0)$ during the micro-dynamics, which ultimately determines the direction and magnitude of tumour boundary movement at macro-scale.

accounting on the relative contribution brought to the ECM degradation of each of the corresponding dyadic cubes. Thus the movement magnitude in direction $\eta_{\epsilon Y}$ is given by

$$\xi_{\epsilon Y(x)} := \sum_{k \in \mathcal{I}_{\epsilon Y}^*} \frac{\int_{\mathcal{D}_k} m(z, \tau_f) dz}{\sum_{k \in \mathcal{I}_{\epsilon Y}^*} \int_{\mathcal{D}_k} m(z, \tau_f) dz} \|\vec{x}y_k\|_2. \quad (2.22)$$

Therefore, as the tumour boundary relocation induced by the micro-dynamics on each ϵY is represented at macro-scale through the movement of the boundary midpoint $x_{\epsilon Y}^*$, in the context that enough but not complete ECM degradation occurs within $\epsilon Y \setminus \Omega(t_0)$ (tissue condition that is detailed and explored in full in [35]), we have that $x_{\epsilon Y}^*$ exercises a relocation to a new position $\widetilde{x}_{\epsilon Y}^*$ that is given by

$$\widetilde{x}_{\epsilon Y}^* = x_{\epsilon Y}^* + \xi_{\epsilon Y(x)} \frac{\widetilde{\eta}_{\epsilon Y}}{\|\widetilde{\eta}_{\epsilon Y}\|_2}, \quad (2.23)$$

where

$$\widetilde{\eta}_{\epsilon Y} := \sum_{k \in \mathcal{I}_{\epsilon Y}^*} \left(\int_{\mathcal{D}_k} m(z, \tau_f) dz \right) (y_k - x_{\epsilon Y}^*), \quad (2.24)$$

and is illustrated through the dark blue arrow in Figure 2. Thus, a law for macro-scale tumour boundary movement is this way induced by the MDEs micro-dynamics, enabling us to capture the evolution

of the tumour boundary over the time interval $[t_0, t_0 + \Delta t]$ from its state $\Omega(t_0)$ at t_0 to a new spatial configuration at $\Omega(t_0 + \Delta t)$ at $t_0 + \Delta t$. This relocated domain $\Omega(t_0 + \Delta t)$ allows the initiation of the dynamics on the next time interval $[t_0, t_0 + \Delta t]$ where the tumour-oncolytic virus interaction continues its proceedings.

2.4. Brief summary of the multiscale model

In summary, the multiscale moving boundary model that we obtained for the tumour–OV interaction (schematically illustrated in Figure 2) is structured as follows,

the tumour-OV
macro-dynamics:

$$\frac{\partial c_p}{\partial t} = D_{c_p} \Delta c_p - \varphi_{c_p}(\mathbf{u}) + \mu_p c_p (1 - \rho(\mathbf{u})) - \varrho_p c_p v + \lambda_{c_p, c_m}, \quad (2.25a)$$

$$\frac{\partial i_p}{\partial t} = D_{i_p} \Delta i_p - \varphi_{i_p}(\mathbf{u}) + \varrho_p c_p v - \delta_{i_p} i_p, \quad (2.25b)$$

$$\frac{\partial c_m}{\partial t} = D_{c_m} \Delta c_m - \nabla \cdot (c_m \mathcal{A}_{c_m}) + \mu_m c_m (1 - \rho(\mathbf{u})) - \varrho_m c_m v + \lambda_{c_m, c_p}, \quad (2.25c)$$

$$\frac{\partial i_m}{\partial t} = D_{i_m} \Delta i_m - \varphi_{i_m}(\mathbf{u}) + \varrho_m c_m v - \delta_{i_m} i_m, \quad (2.25d)$$

$$\frac{\partial e}{\partial t} = -e(\alpha_{c_p} c_p + \alpha_{i_p} i_p + \alpha_{c_m} c_m + \alpha_{i_m} i_m) + \mu_2 e (1 - \rho(\mathbf{u})), \quad (2.25e)$$

$$\frac{\partial v}{\partial t} = D_v \Delta v - \eta_v \nabla \cdot (v \nabla e) + b_m i_m + b_p i_p - (\varrho_m c_m + \varrho_p c_p) v - \delta_v v, \quad (2.25f)$$

boundary MDEs
micro-dynamics:

$$\frac{\partial m}{\partial \tau} = D_m \Delta m + f_{\varepsilon Y}(z, \tau) \quad (2.25g)$$

The macro-dynamics and micro-dynamics are connected through a double feedback loop enabled by:

- a *top-down* link by which the macro-dynamics induces the source for the micro-dynamics given in Eq (2.18).
- a *bottom-up* link by which the MDEs micro-dynamics induces and determines the law for the macro-scale tumour boundary movement.

3. Computational approach

The numerical approach and computational implementation of the novel multiscale moving boundary model require a number of steps that build on the multiscale moving boundary computational framework initially introduced by [35] and further expanded in [34, 47].

3.1. Brief overview of the multiscale computational approach

Macro-scale computations. The maximal macro-scale tissue domain $Y \subset \mathbb{R}^2$, where the tumour-OV interacting macro-dynamics Eq 2.25(a)–(f) takes place, is considered here to be $Y := [0, 4] \times [0, 4]$

and is discretised uniformly using a spatial step size $\Delta x = \Delta y := h$, with $h > 0$. Let's denote by Y^d the discretised Y , i.e., $Y^d := \{(x_i^1, x_j^2)\}_{i,j=1\dots N}$, with $N = \lceil 4/h \rceil + 1$. Further, as the macro-dynamics Eq 2.25(a)–(f) is addressed only on the expanding tumour domain $\Omega(t) \subset Y$, for convenience, for any $t > 0$, we denote the discretised tumour domain by $\Omega^d(t)$ (i.e., $\Omega^d(t) = Y^d \cap \Omega(t)$) and the discretised tumour boundary by $\partial\Omega^d(t)$ (i.e., the frontier of $\Omega^d(t)$ is $\partial\Omega^d(t)$). To carry out the computations exclusively on the expanding tumour, the numerical scheme that we developed here involves a method of lines-type approach combined with a non-local predictor corrector time-marching method introduced in [47] (and, for completeness, summarised also in Appendices A and B). Finally, as the tumour progresses, $\Omega^d(t)$ is appropriately expanded by activating and including within tumour domain the new points invaded by cancer within Y^d .

Approximating the micro-dynamics and its *top-down* and *bottom-up* links with the tumour–OV macro-dynamics. At any instance of time t_0 , we consider that the cell-scale covering bundle $\{\epsilon Y\}_{\epsilon Y \in \mathcal{P}_\epsilon(t_0)}$ of the discretised tumour interface $\partial\Omega^d(t_0)$ consists of overlapping squares ϵY of micro-scale size $\epsilon := 2h$, which are centred at each of the tumour interface spatial node $(x_s^1, x_p^2) \in \partial\Omega^d(t_0)$, i.e.,

$$\{\epsilon Y\}_{\epsilon Y \in \mathcal{P}_\epsilon(t_0)} = \left\{ \mathbf{B}_{\|\cdot\|_\infty}((x_s^1, x_p^2), \epsilon/2) \mid (x_s^1, x_p^2) \in \partial\Omega^d(t_0) \right\}$$

where $\|\cdot\|_\infty$ is the usual ∞ -norm, and $\mathbf{B}_{\|\cdot\|_\infty}((x_s^1, x_p^2), \epsilon/2) := \{(z^1, z^2) \in \mathbb{R}^2 \mid \|(x_s^1, x_p^2) - (z^1, z^2)\|_\infty \leq \epsilon/2\}$ is the closed ball of radius $\epsilon/2$. By adopting a similar approach to the one introduced in [35], we use using bilinear shape functions to calculate the MDE source given by Eq (2.18) on each micro-domain ϵY . To solve MDEs micro-dynamics Eq (2.25g), we use backward Euler in time combined with central differences for the spatial discretisation. After finding the MDE distribution $m(z, \tau)$, with $(z, \tau) \in \epsilon Y \times [0, \Delta t]$, we follow the modelling and computational approach introduced in [35] to determine the direction $\eta_{\epsilon Y}$ and displacement magnitude $\xi_{\epsilon Y}$ for the movement of the tumour boundary $\partial\Omega(t_0) \cap \epsilon Y$ that is captured by each micro-domain $\epsilon Y := \mathbf{B}_{\|\cdot\|_\infty}((x_s^1, x_p^2), \epsilon)$ and is represented trough the movement of its midpoint $(x_s^1, x_p^2) \in \partial\Omega^d(t_0)$. Finally, we use these movement characteristics induced from the micro-dynamics (i.e., $\eta_{\epsilon Y}$ and $\xi_{\epsilon Y}$, $\forall \epsilon Y \in \mathcal{P}_\epsilon(t_0)$) to proceed with the corresponding global relocation of the macro-scale tumour boundary $\partial\Omega^d(t_0)$ to its new spatial configuration $\partial\Omega^d(t_0 + \Delta t)$, which emerges due to the multiscale tumour evolution over the time interval $[t_0, t_0 + \Delta t]$.

3.2. Local vs non-local directed migration due to cell adhesion

In our numerical experiments, we explore the multiscale model dynamics on three distinct local and non-local scenarios that we consider within the macro-dynamics Eq 2.25(a)–(f) for the directed migration due to cell adhesion for cancer cell subpopulations c_p , i_p , and i_m . Specifically, we consider the following cases:

1. The cell-adhesion interactions for both the uninfected proliferative subpopulation c_p and for the infected subpopulations i_p , and i_m are considered to be local of haptotactic type, i.e., in the coupled macro-dynamics in Eq 2.25(a)–(f) we have $\varphi_{c_p}(\mathbf{u}) = \eta_{c_p} \nabla \cdot (c_p \nabla e)$, $\varphi_{i_p}(\mathbf{u}) = \eta_{i_p} \nabla \cdot (i_p \nabla e)$, and $\varphi_{i_m}(\mathbf{u}) = \eta_{i_m} \nabla \cdot (i_m \nabla e)$. Thus, the macro-dynamics Eq 2.25(a)–(f) is in this case of the form:

$$\frac{\partial c_p}{\partial t} = D_{c_p} \Delta c_p - \eta_{c_p} \nabla \cdot (c_p \nabla e) + \mu_p c_p (1 - \rho(\mathbf{u})) - \varrho_p c_p v + \lambda_{c_p, c_m}, \quad (3.1a)$$

$$\frac{\partial i_p}{\partial t} = D_{i_p} \Delta i_p - \eta_{i_p} \nabla \cdot (i_p \nabla e) + \varrho_p c_p v - \delta_{i_p} i_p, \quad (3.1b)$$

$$\frac{\partial c_m}{\partial t} = D_{c_m} \Delta c_m - \nabla \cdot (c_m \mathcal{A}_{c_m}) + \mu_m c_m (1 - \rho(\mathbf{u})) - \varrho_m c_m v + \lambda_{c_m, c_p}, \quad (3.1c)$$

$$\frac{\partial i_m}{\partial t} = D_{i_m} \Delta i_m - \eta_{i_m} \nabla \cdot (i_m \nabla e) + \varrho_m c_m v - \delta_{i_m} i_m, \quad (3.1d)$$

$$\frac{\partial e}{\partial t} = -e(\alpha_{c_p} c_p + \alpha_{i_p} i_p + \alpha_{c_m} c_m + \alpha_{i_m} i_m) + \mu_2 e (1 - \rho(\mathbf{u})), \quad (3.1e)$$

$$\frac{\partial v}{\partial t} = D_v \Delta v - \eta_v \nabla \cdot (v \nabla e) + b_m i_m + b_p i_p - (\varrho_m c_m + \varrho_p c_p) v - \delta_v v, \quad (3.1f)$$

with results for this case shown in Figure 4.

2. The cell-adhesion interactions for the uninfected proliferative subpopulation c_p are considered now to be non-local, while the infected subpopulations i_p , and i_m are still considered to be local of haptotactic type. Hence, in the coupled macro-dynamics in Eq 2.25(a)–(f) we have $\varphi_{c_p}(\mathbf{u}) = \nabla \cdot (c_p \mathcal{A}_{c_p}(\cdot, \cdot, \mathbf{u}(\cdot, \cdot)))$, while $\varphi_{i_p}(\mathbf{u}) = \eta_{i_p} \nabla \cdot (i_p \nabla e)$, and $\varphi_{i_m}(\mathbf{u}) = \eta_{i_m} \nabla \cdot (i_m \nabla e)$. Thus, the macro-dynamics Eq 2.25(a)–(f) is in this case of the form:

$$\frac{\partial c_p}{\partial t} = D_{c_p} \Delta c_p - \nabla \cdot (c_p \mathcal{A}_{c_p}(\cdot, \cdot, \mathbf{u}(\cdot, \cdot))) + \mu_p c_p (1 - \rho(\mathbf{u})) - \varrho_p c_p v + \lambda_{c_p, c_m}, \quad (3.2a)$$

$$\frac{\partial i_p}{\partial t} = D_{i_p} \Delta i_p - \eta_{i_p} \nabla \cdot (i_p \nabla e) + \varrho_p c_p v - \delta_{i_p} i_p, \quad (3.2b)$$

$$\frac{\partial c_m}{\partial t} = D_{c_m} \Delta c_m - \nabla \cdot (c_m \mathcal{A}_{c_m}) + \mu_m c_m (1 - \rho(\mathbf{u})) - \varrho_m c_m v + \lambda_{c_m, c_p}, \quad (3.2c)$$

$$\frac{\partial i_m}{\partial t} = D_{i_m} \Delta i_m - \eta_{i_m} \nabla \cdot (i_m \nabla e) + \varrho_m c_m v - \delta_{i_m} i_m, \quad (3.2d)$$

$$\frac{\partial e}{\partial t} = -e(\alpha_{c_p} c_p + \alpha_{i_p} i_p + \alpha_{c_m} c_m + \alpha_{i_m} i_m) + \mu_2 e (1 - \rho(\mathbf{u})), \quad (3.2e)$$

$$\frac{\partial v}{\partial t} = D_v \Delta v - \eta_v \nabla \cdot (v \nabla e) + b_m i_m + b_p i_p - (\varrho_m c_m + \varrho_p c_p) v - \delta_v v, \quad (3.2f)$$

with results for this case shown in Figure 5(a).

3. Finally, all the cell-adhesion interactions for both the uninfected proliferative subpopulation c_p and for the infected subpopulations i_p , and i_m are considered to be non-local, i.e., in the coupled macro-dynamics in Eq 2.25(a)–(f) we have $\varphi_{c_p}(\mathbf{u}) = \nabla \cdot (c_p \mathcal{A}_{c_p}(\cdot, \cdot, \mathbf{u}(\cdot, \cdot)))$, $\varphi_{i_p}(\mathbf{u}) = \nabla \cdot (i_p \mathcal{A}_{i_p}(\cdot, \cdot, \mathbf{u}(\cdot, \cdot)))$, and $\varphi_{i_m}(\mathbf{u}) = \nabla \cdot (i_m \mathcal{A}_{i_m}(\cdot, \cdot, \mathbf{u}(\cdot, \cdot)))$. Thus, the macro-dynamics Eq 2.25(a)–(f) is in this case of the form:

$$\frac{\partial c_p}{\partial t} = D_{c_p} \Delta c_p - \nabla \cdot (c_p \mathcal{A}_{c_p}) + \mu_p c_p (1 - \rho(\mathbf{u})) - \varrho_p c_p v + \lambda_{c_p, c_m}, \quad (3.3a)$$

$$\frac{\partial i_p}{\partial t} = D_{i_p} \Delta i_p - \nabla \cdot (i_p \mathcal{A}_{i_p}) + \varrho_p c_p v - \delta_{i_p} i_p, \quad (3.3b)$$

$$\frac{\partial c_m}{\partial t} = D_{c_m} \Delta c_m - \nabla \cdot (c_m \mathcal{A}_{c_m}) + \mu_m c_m (1 - \rho(\mathbf{u})) - \varrho_m c_m v + \lambda_{c_m, c_p}, \quad (3.3c)$$

$$\frac{\partial i_m}{\partial t} = D_{i_m} \Delta i_m - \nabla \cdot (i_m \mathcal{A}_{i_m}) + \varrho_m c_m v - \delta_{i_m} i_m, \quad (3.3d)$$

$$\frac{\partial e}{\partial t} = -e(\alpha_{c_p} c_p + \alpha_{i_p} i_p + \alpha_{c_m} c_m + \alpha_{i_m} i_m) + \mu_2 e(1 - \rho(\mathbf{u})), \quad (3.3e)$$

$$\frac{\partial v}{\partial t} = D_v \Delta v - \eta_v \nabla \cdot (v \nabla e) + b_m i_m + b_p i_p - (\varrho_m c_m + \varrho_p c_p) v - \delta_v v, \quad (3.3f)$$

with results for this case shown in Figure 5(b).

3.3. Initial conditions

The initial conditions for the uninfected proliferative cancer cell population, $c_p(x, 0)$ is chosen to describe a small localised pre-existing tumour aggregation. This is given by the following equations:

$$c_p^0(x) = 0.5 \left(\exp\left(-\frac{\|x - (2, 2)\|_2^2}{2h}\right) - \exp(-3.0625) \right) (\chi_{\mathbf{B}((2,2), 0.5-\gamma)} * \psi_\gamma), \quad \forall x \in Y, \quad (3.4)$$

whose plot is shown in Figure 3(a). Here $\psi_\gamma : \mathbb{R}^N \rightarrow \mathbb{R}_+$ is the usual standard mollifier of radius $\gamma \ll \frac{\Delta x}{3}$ given by

$$\psi_\gamma(x) := \frac{1}{\gamma^N} \psi\left(\frac{x}{\gamma}\right), \quad (3.5)$$

where ψ is the smooth compact support function given by

$$\psi(x) := \begin{cases} \exp\frac{1}{\|x\|_2^2 - 1} & \text{if } \|x\|_2 < 1, \\ 0 & \text{otherwise.} \end{cases} \quad (3.6)$$

Moreover, we assume that the tumour is detected early enough so that migration is not initiated at the start of these simulations, and thus

$$c_m^0(x) = 0, \quad \forall x \in Y. \quad (3.7)$$

Also, since there is no infection at this stage, we assume that both infected proliferative ($i_p(x, 0)$) and migrating ($i_m(x, 0)$) cancer cells are zero:

$$i_p^0(x) = 0, \quad \text{and} \quad i_m^0(x) = 0, \quad \forall x \in Y. \quad (3.8)$$

Furthermore, the initial condition for the ECM density, $e(x, 0)$, is represented by an arbitrarily chosen heterogeneous pattern described by the following equations (as in [47])

$$e(x, 0) = \frac{1}{2} \min\{h(\zeta_1(x), \zeta_2(x)), 1 - c_p^0(x)\}, \quad (3.9)$$

and is shown in Figure 3(b). Here, we have

$$\begin{aligned} h(\zeta_1(x), \zeta_2(x)) &:= \frac{1}{2} + \frac{1}{4} \sin(\xi \zeta_1(x) \zeta_2(x))^3 \cdot \sin\left(\xi \frac{\zeta_2(x)}{\zeta_1(x)}\right), \\ (\zeta_1(x), \zeta_2(x)) &:= \frac{1}{3}(x + \frac{3}{2}) \in [0, 1]^2, \quad \forall x \in Y, \quad \text{and} \quad \xi = 7\pi. \end{aligned} \quad (3.10)$$

While other types of heterogeneous ECM patterns could be considered (see [53]), here we focus our attention to explore cancer-viral dynamics on this particular ECM pattern.

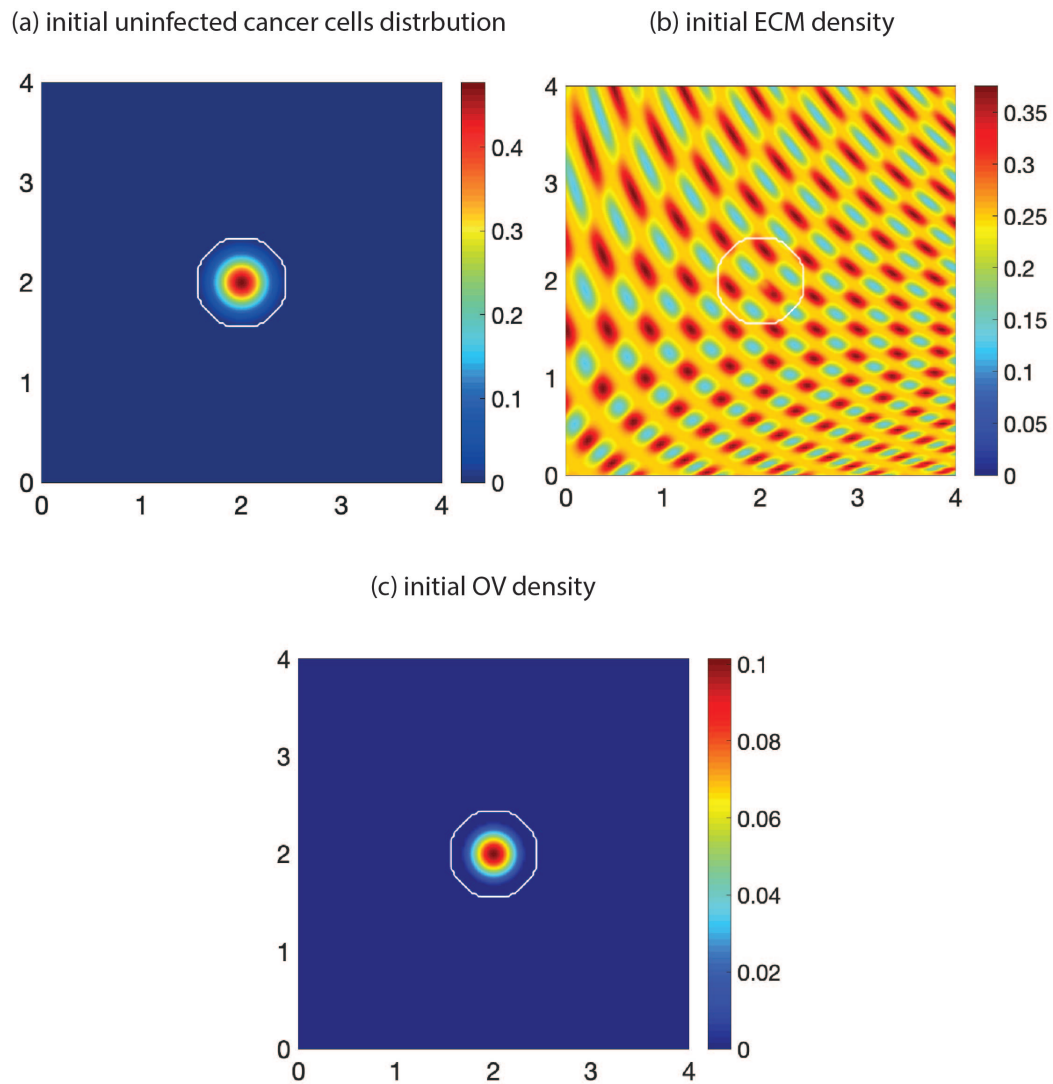


Figure 3. Initial conditions used for the numerical simulations: (a) proliferative uninfected cancer cells density c_p , as described by Eq (3.4); (b) ECM density, as described by Eq (3.9); (c) OV density, as described by Eq (3.11). The white curve indicates the tumour boundary.

Finally, the initial conditions for the OV population, $v(x, 0)$ is chosen to describe one single injection in the middle of the tumour aggregation, as in [34]. This is described by the equation

$$v^0(x) = \Phi(x) \cdot \theta(v), \quad (3.11)$$

where

$$\begin{aligned} \Phi(x) &= \frac{1}{8} \left(\exp\left(-\frac{\|x - (2, 2)\|_2^2}{2h}\right) - \exp(-1.6625) \right), \\ \text{and} \\ \theta(v) &= \begin{cases} 1 & \text{if } \Phi(x) > 5 \times 10^{-5}, \\ 0 & \text{otherwise.} \end{cases} \end{aligned} \quad (3.12)$$

In computations, the initial condition is smoothed out on the frontier of the viral density support $\Gamma_v := \partial\{x \in Y \mid v^0(x) > 0\}$ via the averaging

$$v(x^1, x^2) = \frac{1}{8} \left(-v(x^1, x^2) + \sum_{i,j \in \{-1,0,1\}} v(x^1 + ih, x^2 + jh) \right), \quad \forall (x^1, x^2) \in \Gamma_v. \quad (3.13)$$

4. Results

The numerical results presented in this Section are obtained with the parameter values described in Table 1 which, for convenience we call them ‘baseline parameters’. Whenever we vary these parameters, we state clearly the new values we use for those simulations. Note that these baseline parameters are based on other papers or on our own estimates. For instance, using the GOG hypothesis, we estimated that D_{c_p} is likely much smaller than D_{c_m} . Since we could not find an exact value for D_{c_p} (D_{c_m} was assumed to be 0.00035, as in [43]), we arbitrarily estimated $D_{c_p} = 10^{-5}$.

We start in Section 4.1 by investigating numerically the impact of local vs. nonlocal approaches used to describe the cell-cell and cell-matrix adhesion flux. Then, in Section 4.2, we investigate the impact of varying the adhesion strength in the non-local cell flux. Following that we focus on the system of Eq (3.1) without haptotaxis for c_p (*i.e.*, $\eta_{c_p} = 0$), to investigate the impact of varying different parameters: in Section 4.3 we vary the impact of transition rate between migrating and proliferative cells, in Section 4.4 we vary the impact of OVs infection rate, and in Section 4.5 we vary the impact of OVs replication rate.

4.1. The importance of cell-cell and cell-matrix adhesion: Local vs non-local approaches

First, we focus on model (3.1), described in detail in Section 3.2. In Figure 4(a) we show the dynamics of our multiscale model in the absence of haptotactic terms for the proliferative uninfected cells ($\eta_{c_p} = 0$), while in Figure 4(b) we show the dynamics of this model in the presence of such haptotactic terms (where $\eta_{c_p} = 0.00285$, as given in Table 1). We can see that, for the parameter values used in these simulations, there is no difference in the spatial distribution of migrating uninfected or infected cancer cells between panels (a) and (b). However, the addition of haptotactic movement impacts the spatial distribution of proliferative uninfected cancer cells, leading to a more localised cancer cells distribution.

Table 1. Baseline parameters values used for our multiscale computations.

Param.	Value	Description	Reference
D_{c_m}	0.00035	Uninfected migrating cancer cell diffusion coefficient	[43]
D_{i_m}	0.0054	Infected migrating cancer cell diffusion coefficient	[54]
D_{i_p}	0.00054	Infected proliferative cancer cell diffusion coefficient	Estimated
D_{c_p}	10^{-5}	Uninfected proliferative cancer cell diffusion coefficient	Estimated
D_v	0.0036	Constant diffusion coefficient for OV	[54]
η_{c_p}	0.00285	Infected proliferative cancer cell haptotaxis coefficient	Estimated
η_{i_m}	0.0285	Infected migrating cancer cell haptotaxis coefficient	[29]
η_{i_p}	0.00285	Infected proliferative cancer cell haptotaxis coefficient	Estimated
η_v	0.0285	OV haptotaxis coefficient	[29]
μ_m	0.5	Proliferation rate for uninfected migrating cancer cells	[41]
μ_p	0.75	Proliferation rate for uninfected proliferative cancer cells	[41]
$S_{c_m c_m}$	0.1	Maximum rate of cell-cell adhesion strength	[44]
$S_{c_p c_p}$	0.05	Maximum rate of cell-cell adhesion strength	Estimated
$S_{i_m i_m}$	0.1	Maximum rate of cell-cell adhesion strength	Estimated
$S_{i_p i_p}$	0.05	Maximum rate of cell-cell adhesion strength	Estimated
$S_{c_m e}$	0.5	Rate of Cell-ECM adhesion strength	[55]
$S_{c_p e}$	0.001	Rate of Cell-ECM adhesion strength	Estimated
$S_{i_m e}$	0.5	Rate of Cell-ECM adhesion strength	Estimated
$S_{i_p e}$	0.001	Rate of Cell-ECM adhesion strength	Estimated
ω_1	0.1	Rate of switching from proliferative state (c_p) to migration state (c_m)	Estimated
ω_2	0.4	Rate of switching from migration (c_m) to proliferative state (c_p).	Estimated
α_{c_m}	0.075	ECM degradation rate by uninfected cancer cells	Estimated
α_{i_m}	$\frac{\alpha_{c_m}}{2}$	ECM degradation rate by infected cancer cells	[29]
α_{c_p}	0.075	ECM degradation rate by uninfected cancer cells	Estimated
α_{i_p}	$\frac{\alpha_{c_m}}{2}$	ECM degradation rate by infected cancer cells	Estimated
μ_2	0.02	Remodelling term coefficient	[34]
ϱ_m	0.079	Infection rate of c_m cells by OV	[29]
ϱ_p	0.079	Infection rate of cells by OV	Estimated
δ_{i_m}	0.05	Death rate of infected cancer cells	[54]
δ_{i_p}	0.05	Death rate of infected cancer cells	Estimated
b_m	40	Replicating rate of OVs in infected cancer cells c_m	Estimated
b_p	40	Replicating rate of OVs in infected cancer cells c_p	Estimated
δ_v	0.05	Death rate of OV	[54]
v_e	1	The fraction of physical space occupied by the ECM	[47]
v_c	1	The fraction of physical space occupied by cancer cells	[47]
γ_{c_m}	1.5	MDEs secretion rate by uninfected cancer cell	[56]
γ_{i_m}	1	MDEs secretion rate by infected cancer cell	[56]
γ_{c_p}	1	MDEs secretion rate by uninfected cancer cell	Estimated
γ_{i_p}	1.5	MDEs secretion rate by infected cancer cell	Estimated
D_m	0.004	MDE diffusion coefficient	[57]

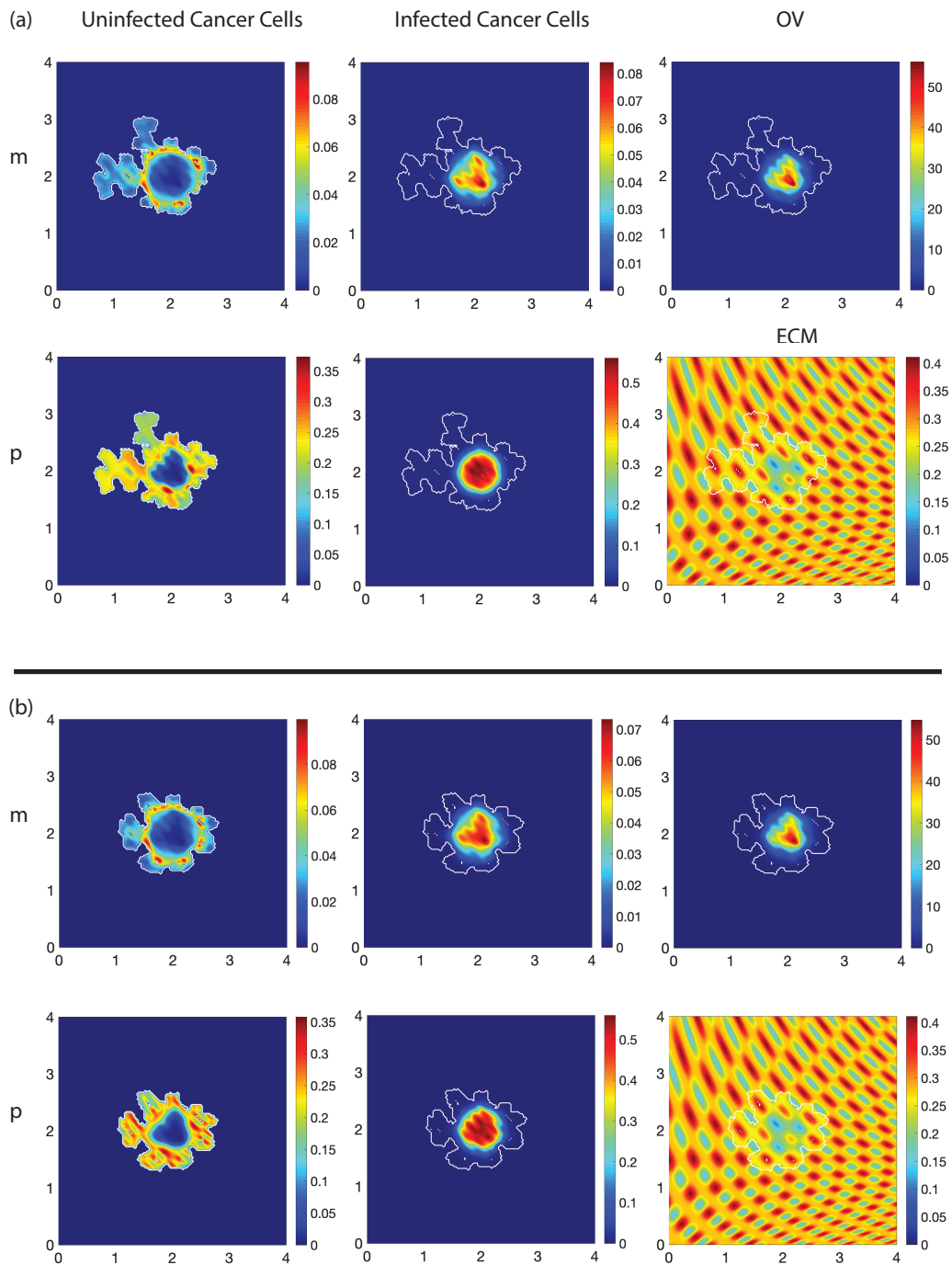


Figure 4. Simulations of system (3.1) using the parameters in Table 1. Here we show cell and virus distributions at micro-macro stage 75. (a) c_p without haptotaxis ($\eta_{c_p} = 0$), (m) migrating cells; (p) proliferative cells. (b) and c_p with haptotaxis ($\eta_{c_p} = 0.00285$).

Next, we investigate numerically the dynamics of models (3.2) and (3.3). In Figure 5(a) we show the dynamics of our multi-scale model (3.2) that has two non-local fluxes c_m and c_p , while in Figure

5(b) we show what happens when we consider non-local fluxes for all cancer cells subpopulations (i.e., model (3.3)). Clearly there is a difference between these results and the previous one. The cancer cells for the case with two non-local fluxes (i.e., for proliferative c_p and migrating c_m cells) are more invasive, but have lower densities compared to the case where we assume four non-local adhesion fluxes. We can also see that the OV density for the case described by model (3.2) (with two nonlocal fluxes) is almost double compared to the OV density for the case described by model (3.3) (with four nonlocal fluxes).

4.2. The impact of adhesion strength

In this subsection we investigate the effect of cell-cell and cell-matrix adhesion strengths for the two non-local subpopulations (i.e., model (3.2)) versus the four non-local subpopulations (i.e., model (3.3)). In [34] the authors studied the impact of different adhesion strengths in a model with one homogeneous cancer population and showed that when cell-cell adhesion strength was lower than cell-matrix adhesion strength it led to larger tumour spread. Since here we focus on two different cancer cell sub-populations (i.e., migrating and proliferative), we assume that cell-cell adhesion strength is lower than cell-matrix adhesion strength for the migrating cancer cells c_m, i_m (to allow for cell migration), and the other way around for the proliferative cancer cells c_p, i_p (to reduce cell migration). The results of numerical simulations with these different adhesion strengths are shown in Figure 5. In this case we see relatively similar tumour spread patterns for (a) model (3.2) with two non-local sub-populations and for (b) model (3.3) with four non-local sub-populations. The only difference is a slight increase in the density for uninfected cancer cells and a decrease in the density of infected cancer cells for the model in sub-panels (b).

Since it is difficult to measure the adhesion strengths for cells with different phenotypes, in Figure 6 we also investigate numerically what happens with tumour and virus spread patterns when we assume that all cancer subpopulations have similar cell-cell adhesion strengths that are lower than their cell-matrix adhesion strengths. In this case we see that the cancer cells show less spatial spread compare to the case in Figure 5. Moreover, the OV (which has the highest density in the middle of the tumour mass) cannot destroy the tumour in that region; this is more evident in sub-panels (b) (for model (3.3) with four non-local sub-populations), where the level of the virus is also very reduced. In sub-panels (a) (for model (3.2) with two non-local sub-populations) we still see a bit of reduction in tumour size in the middle of the tumour region where the level of OV is similar as in Figure 5.

We conclude from these two numerical studies that the magnitudes of cell-cell and cell-matrix adhesion strengths for different cancer cell phenotypes (here migrating and proliferative cells), combined with their local/non-local character, influence significantly the spread of the virus through the tumour.

In the next three sub-sections we return to model (3.1) without haptotaxis for c_p cells (i.e., $\eta_{c_p} = 0$), and investigate the impact of transition rates between migrating and proliferative cell sub-populations, as well as the impact of virus infection and replication rates.

4.3. The impact of transition rates

We return now to model (3.1) without haptotaxis for c_p (i.e., $\eta_{c_p} = 0$), and investigate numerically the impact of varying the transition rates between migrating and proliferating cancer cells, and the

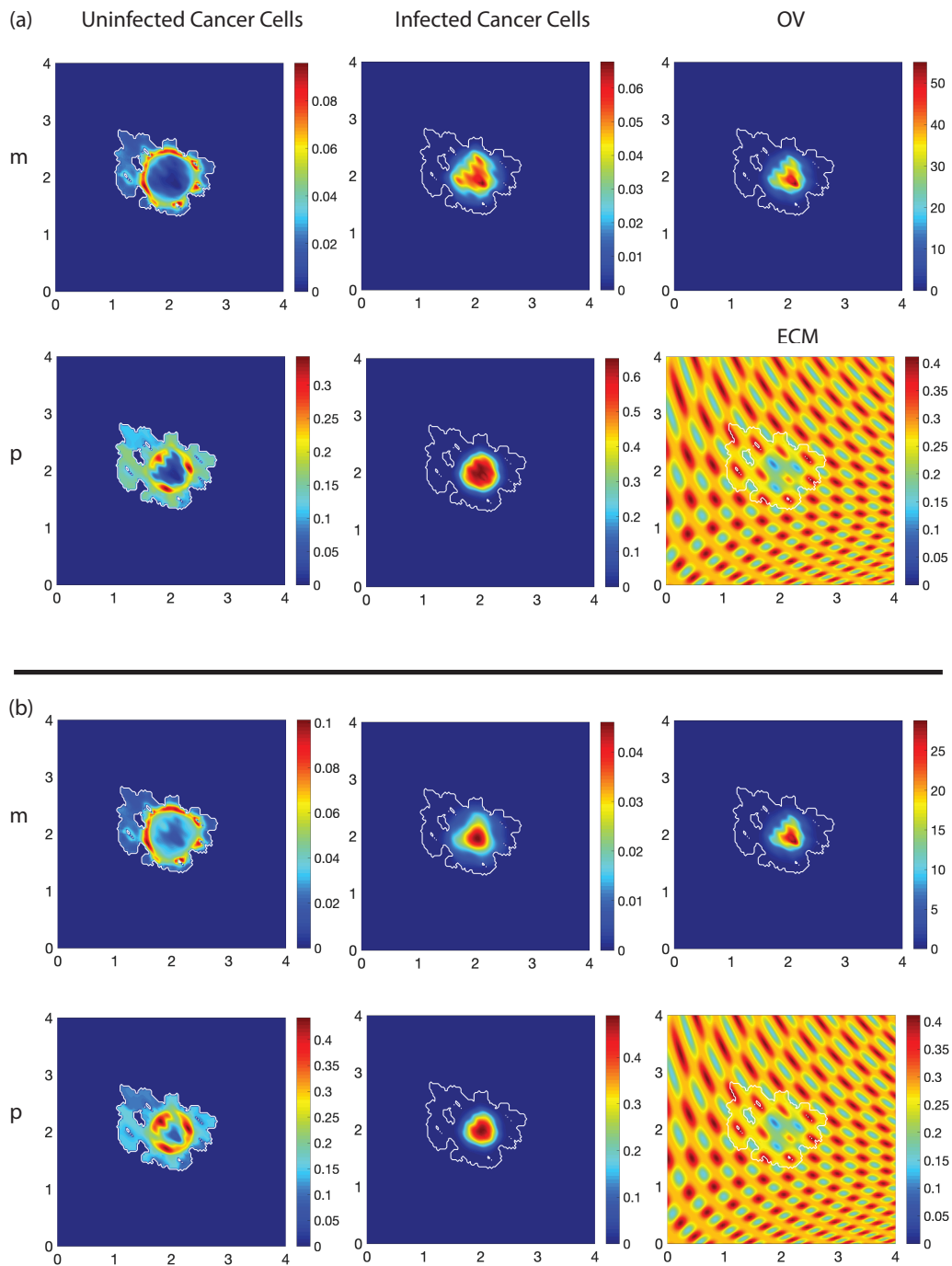


Figure 5. Simulations of systems (3.2) and (3.3) using the parameters in Table 1. Here we show the cell and virus distribution at micro-macro stage 75. Moreover “m” denotes migrating cells, while “p” denotes proliferative cells. (a) Model (3.2): two non-local subpopulation c_m, c_p . (b) Model (3.3): four non-local subpopulations c_m, i_m, c_p, i_p .

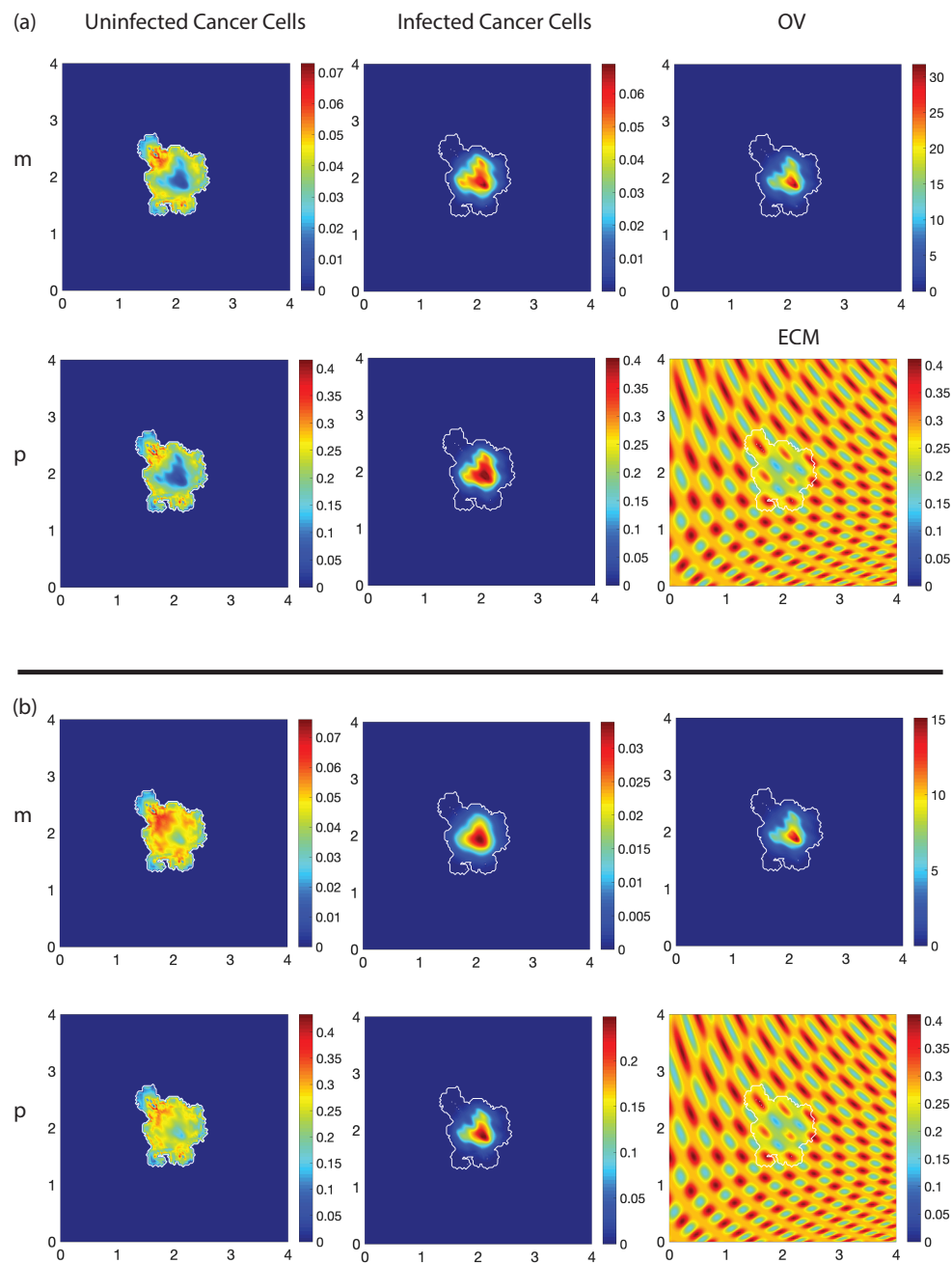


Figure 6. Simulations of systems (3.2) and (3.3) using the parameters in Table 1. Here we show cell and virus distributions at the micro-macro stage 75 with $S_{c_p c_p} = S_{i_p i_p} = S_{c_m c_m} = 0.1$ and $S_{c_p e} = S_{i_p e} = S_{c_m e} = 0.5$. Moreover “m” denotes migrating cells, while “p” denotes proliferative cells. (a) Model (3.2): two non-local sub-population c_m, c_p . (b) Model (3.3): four non-local sub-population c_m, c_p, i_p, i_m .

differences from the baseline results shown before in Figure 4(a). In Figure 7 we investigate the spatial spread of tumour and virus populations when (a) $\omega_2 = \omega_1 = 0.1$, and (b) $\omega_2 = \frac{\omega_1}{4} = 0.025$. We see that decreasing ω_2 leads to an increase in the density of migrating cells (c_m, i_m , in sub-panel (b)) compared to the case in Figure 4(a). Moreover, we see an increase in the spatial spread of the tumour between sub-panel (a) and sub-panel (b) where there are more migrating cancer cells.

4.4. The impact of infection rate

In Figure 8 we investigate the impact of the infection rates of cancer cells by the virus particles for the model (3.1) when we ignore the haptotaxis for c_p (i.e., $\eta_{c_p} = 0$); we compare the results with those in Figure 7(b). In Figure 8(a) we assume that the proliferating cells have a faster infection rates compared to the migrating cells: $\varrho_p = 3\varrho_m = 0.316$. In Figure 8(b) we assume that the migrating cells have a faster infection rates compared to the proliferating cells: $\varrho_m = 3\varrho_p = 0.316$. We see that by increasing the OV infection rate for any cancer subpopulation it leads to an increase viral density, better viral spread and better killing of cancer cells. This cancer-killing effect is slightly more pronounced in sub-panels (a) where $\varrho_p > \varrho_m$.

4.5. The impact of replicating rate of OVs

In Figure 9 we investigate the impact of varying the OV replication rate for model (3.1) without c_p haptotaxis (i.e., $\eta_{c_p} = 0$), and the results are compared to Figure 7(b). When (a) $b_p = 50 \geq b_m = 40$, the impact of increasing b_p by a small amount is more evident on the proliferative cancer population c_p and on the virus density. When (b) $b_p = \frac{b_m}{8} = 5$ and $b_m = 40$, it is clear that decreasing b_p while keeping b_m fixed leads to a very low OV density and a higher density of proliferative cells c_p in the middle of the tumour mass compared to the case (a) when $b_p > b_m$. Compared to the results in Figure 7(b) we deduce that increasing b_p leads to a reduction in c_p but not c_m and an increase in virus v levels, while decreasing b_p leads to an increase in both c_p and c_m and a drastic reduction in virus v levels.

5. Conclusions

In this study we proposed a new multiscale moving boundary model that considers the local/non-local interactions between cancer cells and ECM, as well as the infections of cancer cells with oncolytic viruses (OV), all in the context of the *go or grow* hypothesis. This model generalises the previous studies in [34] (that focused on nonlocal multi-scale moving boundary models for oncolytic virotherapies in the context of a homogeneous cancer population) and [29, 58] (that focused on local multiscale moving boundary models for oncolytic virotherapies in the context of a homogeneous cancer population). Here, we consider a heterogeneous cancer cell population formed of two sub-populations: mainly-migrating and mainly-proliferative cells.

Using this new model, we investigated not only the impact of different cell-cell and cell-ECM interaction strengths on the overall spread of cancer cells and OVs (see Figures 4–6), but also the effect of changes in the transition rates between the migrating and proliferative cells (see Figure 7), as well as the effects of varying the infection rates of different cancer cells (Figure 8), and the proliferation rates of viruses inside different cancer cells (Figure 9). First, we have seen that the magnitudes of cell-cell and cell-matrix adhesion strengths for different cancer cell phenotypes (i.e., migrating and

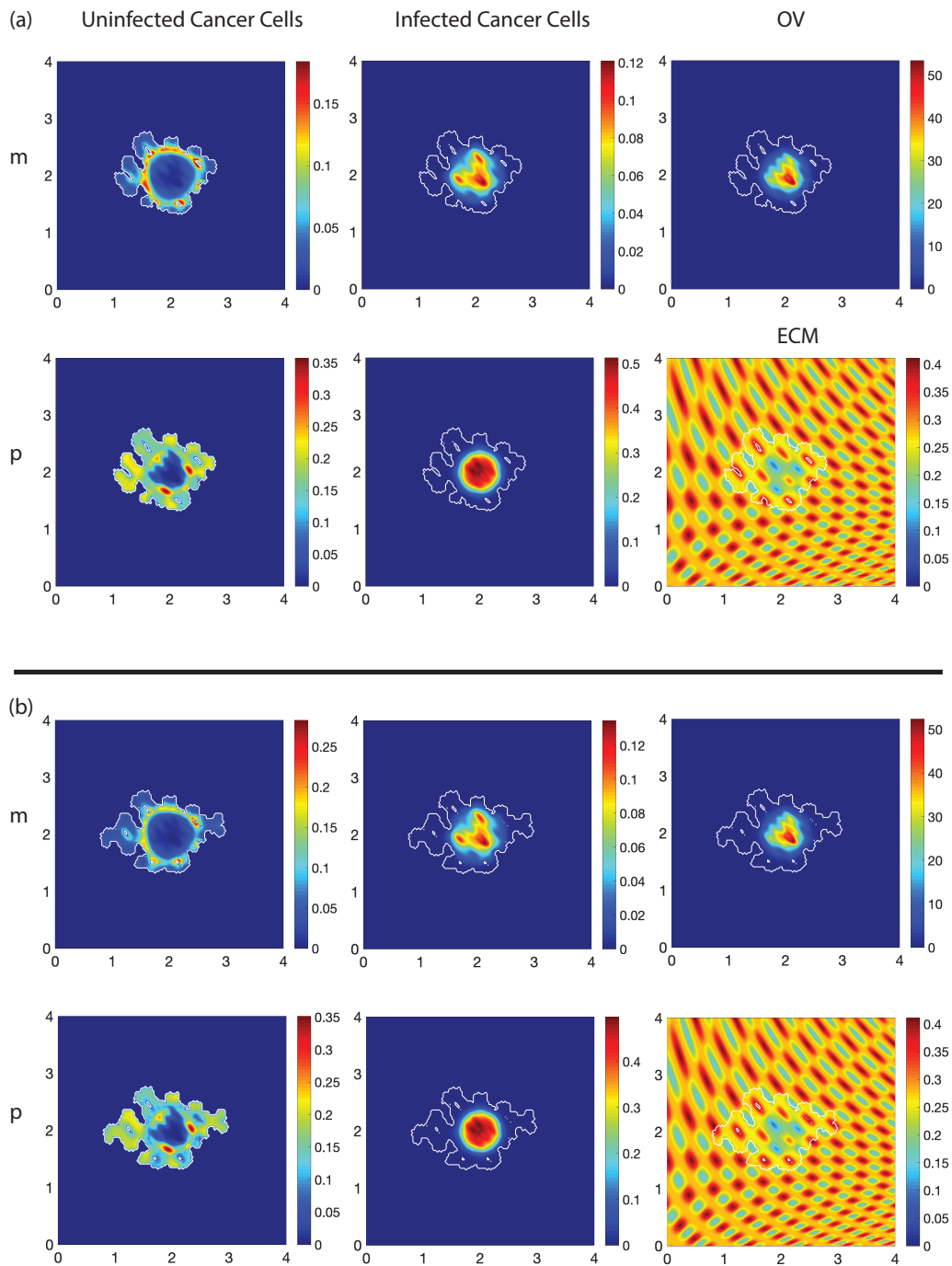


Figure 7. Simulations of system (3.1) using the parameters in Table 1 without haptotaxis for c_p (i.e., $\eta_{c_p} = 0$). Here we show the cell and virus distributions at the micro-macro stage 75. We denote by “m” the migrating cells, and by “p” the proliferative cells. (a) $\omega_2 = \omega_1 = 0.1$. (b) $\omega_2 = \frac{\omega_1}{4} = 0.025$.

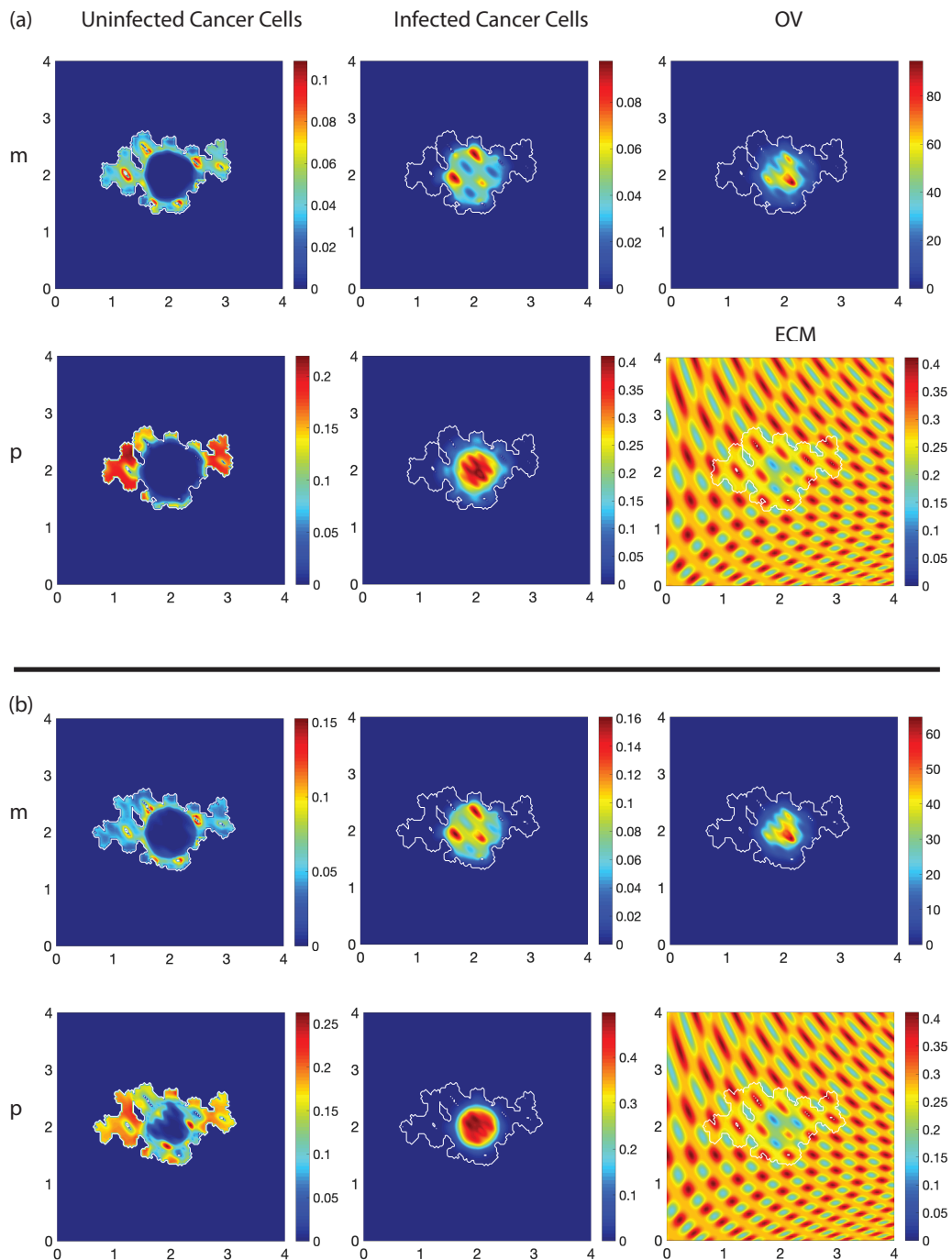


Figure 8. Simulations of system (3.1) without haptotaxis for c_p (i.e., $\eta_{c_p} = 0$), using the parameters in Table 1 and $\omega_2 = \frac{\omega_1}{4} = 0.025$ (to compare the results with those in Figure 7(b)). Here we show the cell and virus distribution at micro-macro stage 75. Also, we denote by “m” the migrating cells, and by “p” the proliferative cells. (a) $\varrho_p = 3\varrho_m$. (b) $\varrho_m = 3\varrho_p$.

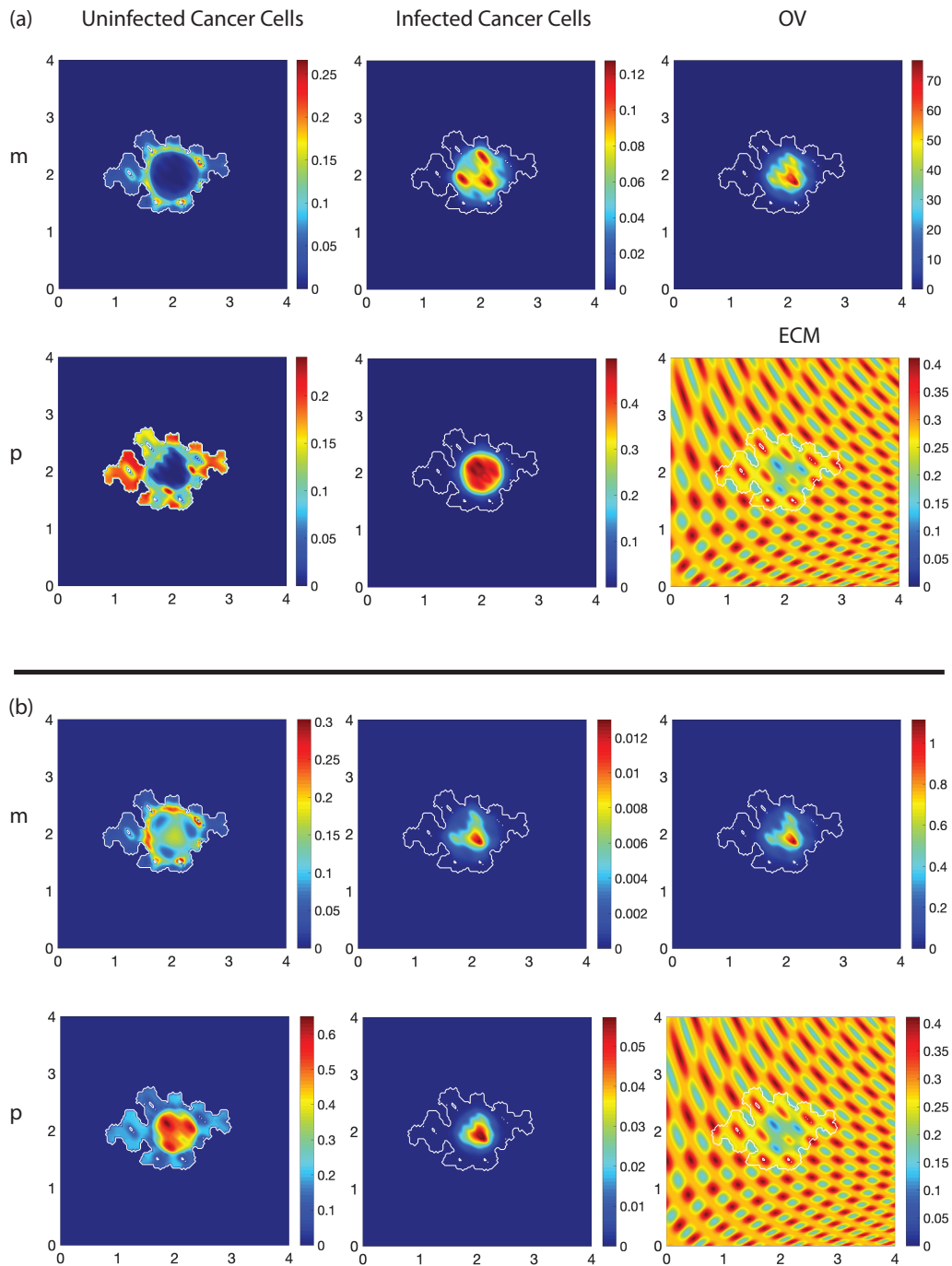


Figure 9. Simulations of system (3.1) without haptotaxis for c_p (i.e., $\eta_{c_p} = 0$), using the parameters in Table 1 and $\omega_2 = \frac{\omega_1}{4} = 0.025$. Here we show the cell and virus distributions at micro-macro stage 75. Also we denote by “m” the migrating cells and by “p” the proliferative cells. (a) $b_p = 50$ and $b_m = 40$; (b) $b_p = \frac{b_m}{8}$ and $b_m = 40$.

proliferative cells), combined with their local/non-local character, influence significantly the spread of the virus through the tumour. Second, we have seen that the killing of cancer cells by the OVs is slightly more pronounced when the proliferating cells have a faster infection rate compared to the migrating cells (i.e., $\varrho_p > \varrho_m$). This suggests that giving the virus during a certain time interval, when the majority of cells in the solid tumour are in a proliferative phase, might eventually lead to better cancer killing. Finally, we have seen that viral replication inside proliferating cells (and viral burst size from these cells) might affect in some cases not only the density of proliferative cells but also the density of migrating cells. For example, when $b_p > b_m$, the migrating cells do not seem to be greatly impacted; however, for $b_p < b_m$, the migrating cells are impacted.

To conclude, we emphasise that the heterogeneity of solid cancers (formed of sub-populations of cells with different phenotypes; e.g., mainly-migrating and mainly-proliferative cells) might impact the success of oncolytic therapies, where the virus needs to spread throughout the tumour to be able to eliminate it. We would also like to suggest that one possible explanation for the contradictory experimental results in regard to validity of the *go or grow* hypothesis for various cancer cell lines (see our discussion in the Introduction) might be related to the differences in the heterogeneity of tumours for these different cell lines. However, this hypothesis will have to be tested experimentally in the future.

Acknowledgments

The first author would like to acknowledge the financial support received from the Saudi Arabian Cultural Bureau in the UK on behalf of Taibah University, Medina, Saudi Arabia.

Conflict of interest

All authors declare no conflicts of interest in this paper.

References

1. A. Corcoran, R. F. Del Maestro, Testing the “go or grow” hypothesis in human medulloblastoma cell lines in two and three dimensions, *Neurosurgery*, **53** (2003), 174–185.
2. A. Giese, M. A. Loo, N. Tran, D. Haskett, S. W. Coons, M. E. Berens, Dichotomy of astrocytoma migration and proliferation, *Int. J. Cancer*, **67** (1996), 275–282.
3. A. Giese, R. Bjerkvig, M. E. Berens, M. Westphal, Cost of migration: invasion of malignant gliomas and implications for treatment, *J. Clin. Oncol.*, **21** (2003), 1624–1636.
4. K. S. Hoek, O. M. Eichhoff, N. C. Schlegel, U. Dobbeling, N. Kobert, L. Schaerer, et al., In vivo switching of human melanoma cells between proliferative and invasive states, *Cancer Res.*, **68** (2008), 650–656.
5. J. Godlewski, M. O. Nowicki, A. Bronisz, G. Nuovo, J. Palatini, M. D. Lay, et al., MicroRNA-451 regulates LKB1/AMPK signaling and allows adaptation to metabolic stress in glioma cells, *Mol. Cell*, **37** (2010), 620–632.

6. L. Jerby, L. Wolf, C. Denkert, G. Y. Stein, M. Hilvo, M. Oresic, et al., Metabolic associations of reduced proliferation and oxidative stress in advanced breast cancer, *Cancer Res.*, **72** (2012), 5712–5720.
7. J. Metzcar, Y. Wang, R. Heiland, P. Macklin, A review of cell-based computational modeling in cancer biology, *JCO Clin. Cancer Inf.*, (2019), 1–13.
8. J. A. Gallaher, J. S. Brown, A. R. A. Anderson, The impact of proliferation-migration tradeoffs on phenotypic evolution in cancer, *Sci. Rep.*, **9** (2019), 1–10.
9. M. Tektonidis, H. Hatzikirou, A. Chauvière, M. Simon, K. Schaller, A. Deutsch, Identification of intrinsic in vitro cellular mechanisms for glioma invasion, *J. Theor. Biol.*, **287** (2011), 131–147.
10. T. Garay, É. Juhász, E. Molnár, M. Eisenbauer, A. Czirók, B. Dekan, et al., Cell migration or cytokinesis and proliferation? – Revisiting the “go or grow” hypothesis in cancer cells in vitro, *Exp. Cell Res.*, **319** (2013), 3094–3103.
11. S. T. Vittadello, S. W. McCue, G. Gunasingh, N. K. Haass, M. J. Simpson, Examining go-or-grow using fluorescent cell-cycle indicators and cell-cycle-inhibiting drugs, *Biophys. J.*, **118** (2020), 1243–1247.
12. J. C. L. Alfonso, K. Talkenberger, M. Seifert, B. Klink, A. Hawkins-Daarud, K. R. Swanson, et al., The biology and mathematical modelling of glioma invasion: a review, *J. R. Soc. Interface*, **14** (2017), 20170490.
13. K. Böttger, H. Hatzikirou, A. Chauviere, A. Deutsch, Investigation of the migration/proliferation dichotomy and its impact on avascular glioma invasion, *Math. Model. Nat. Phenom.*, **7** (2012), 105–135.
14. K. Böttger, H. Hatzikirou, A. Voss-Böhme, E. A. Cavalcanti-Adam, M. A. Herrero, A. Deutsch, An emerging Allee effect is critical for tumor initiation and persistence, *PLOS Comput. Biol.*, **11** (2015), e1004366.
15. P. Gerlee, S. Nelander, The impact of phenotypic switching on glioblastoma growth and invasion, *PLoS Comput. Biol.*, **8** (2012).
16. H. Hatzikirou, D. Basanta, M. Simon, K. Schaller, A. Deutsch, ‘Go or Grow’: the key to the emergence of invasion in tumour progression?, *Math. Med. Biol.*, **29** (2012), 49–65.
17. H. N. Weerasinghe, P. M. Burrage, K. Burrage, D. V. Nicolau, Mathematical models of cancer cell plasticity, *J. Oncol.*, (2019), 1–14.
18. Y. Kim, H. Kang, S. Lawler, The role of the miR-451-AMPK signaling pathway in regulation of cell migration and proliferation in glioblastoma, in *Mathematical Models of Tumor-Immune System Dynamics*, Springer, New York, (2014), 25–155.
19. A. V. Kolobov, V. V. Gubernov, A. A. Polezhaev, Autowaves in the model of infiltrative tumour growth with migration-proliferation dichotomy, *Math. Model. Nat. Phenom.*, **6** (2011), 27–38.
20. K. Pham, A. Chauviere, H. Hatzikirou, X. Li, H. M. Byrne, V. Cristini, et al., Density-dependent quiescence in glioma invasion: instability in a simple reaction–diffusion model for the migration/proliferation dichotomy, *J. Biol. Dyn.*, **6** (2012), 54–71.

21. O. Saut, J. B. Lagaert, T. Colin, H. M. Fathallah-Shaykh, A multilayer grow-or-go model for GBM: effects of invasive cells and anti-angiogenesis on growth, *Bull. Math. Biol.*, **76** (2014), 2306–2333.
22. T. L. Stepien, E. M. Rutter, Y. Kuang, Traveling waves of a go-or-grow model of glioma growth, *SIAM J. Appl. Math.*, **78** (2018), 1778–1801.
23. C. Stinner, C. Surulescu, A. Uatay, Global existence for a go-or-grow multiscale model for tumor invasion with therapy, *Math. Model. Methods Appl. Sci.*, **26** (2016), 2163–2201.
24. E. Scribner, O. Saut, P. Province, A. Bag, T. Colin, H. M. Fathallah-Shaykh, Effects of anti-angiogenesis on glioblastoma growth and migration: model to clinical predictions, *PLoS One*, **9** (2014), e115018.
25. A. Zhigun, C. Surulescu, A. Hunt, A strongly degenerate diffusion-haptotaxis model of tumour invasion under the go-or-grow dichotomy hypothesis, *Math. Methods Appl. Sci.*, **41** (2018), 2403–2428.
26. M. A. Lewis, G. Schmitz, Biological invasion of an organism with separate mobile and stationary states: Modeling and analysis, *Forma*, **11** (1996), 1–25.
27. X. Ma, M. E. Schickel, M. D. Stevenson, A. L. Sarang-Sieminski, K. J. Gooch, S. N. Ghadiali, et al., Fibres in the extracellular matrix enable long-range stress transmission between cells, *Biophys. J.*, **104** (2013), 1410–1418.
28. N. J. Armstrong, K. J. Painter, J. A. Sherratt, A continuum approach to modelling cell-cell adhesion, *J. Theor. Biol.*, **243** (2006), 98–113.
29. T. Alzahrani, R. Eftimie, D. Trucu, Multiscale modelling of cancer response to oncolytic viral therapy, *Math. Biosci.*, **310** (2019), 76–95.
30. J. Ahn, M. Chae, J. Lee, Nonlocal adhesion models for two cancer cell phenotypes in a multidimensional bounded domain, *Z. Angew. Math. Phys.*, **72** (2021), 1–28.
31. M. Eckardt, K. J. Painter, C. Surulescu, A. Zhigun, Nonlocal and local models for taxis in cell migration: a rigorous limit procedure, *J. Math. Biol.*, **81** (2020), 1251–1298.
32. R. Alemany, Viruses in cancer treatment, *Clin. Transl. Oncol.*, **15** (2013), 182–188.
33. M. Vähä-Koskela, A. Hinkkanen, Tumor restrictions to oncolytic virus, *Biomedicines*, **2** (2014), 163–194.
34. A. Alsisi, R. Eftimie, D. Trucu, Non-local multiscale approaches for tumour-oncolytic viruses interactions, *Math. Appl. Sci. Eng.*, **99** (2020), 1–27.
35. D. Trucu, P. Lin, M. A. J. Chaplain, Y. Wang, A multiscale moving boundary model Arising in cancer invasion, *Multiscale Model. Simul.*, **11** (2013), 309–335.
36. N. Bhagavathula, A. W. Hanosh, K. C. Nerusu, H. Appelman, S. Chakrabarty, J. Varani, Regulation of E-cadherin and β -catenin by Ca^{2+} in colon carcinoma is dependent on calcium-sensing receptor expression and function, *Int. J. Cancer*, **121** (2007), 1455–1462.
37. U. Cavallaro, G. Christofori, Cell adhesion in tumor invasion and metastasis: loss of the glue is not enough, *Biochim. Biophys. Acta Rev. Cancer*, **1552** (2001), 39–45.
38. J. D. Humphries, Integrin ligands at a glance, *J. Cell Sci.*, **119** (2006), 3901–3903.

39. K. S. Ko, P. D. Arora, V. Bhide, A. Chen, C. A. McCulloch, Cell-cell adhesion in human fibroblasts requires calcium signaling, *J. Cell Sci.*, **114** (2001), 1155–1167.
40. B. P. L. Wijnhoven, W. N. M. Dinjens, M. Pignatelli, E-cadherin-catenin cell-cell adhesion complex and human cancer, *Br. J. Surg.*, **87** (2000), 992–1005.
41. M. A. J. Chaplain, G. Lolas, Mathematical modelling of cancer invasion of tissue: dynamic heterogeneity, *Networks Heterog. Media*, **1** (2006), 399–439.
42. M. J. Oudin, O. Jonas, T. Kosciuk, L. C. Broye, B. C. Guido, J. Wyckoff, et al., Tumor cell-driven extracellular matrix remodeling drives haptotaxis during metastatic progression, *Cancer Discovery*, **6** (2016), 516–531.
43. P. Domschke, D. Trucu, A. Gerisch, M. A. J. Chaplain, Mathematical modelling of cancer invasion: Implications of cell adhesion variability for tumour infiltrative growth patterns, *J. Theor. Biol.*, **361** (2014), 41–60.
44. A. Gerisch, M. A. J. Chaplain, Mathematical modelling of cancer cell invasion of tissue: Local and non-local models and the effect of adhesion, *J. Theor. Biol.*, **250** (2008), 684–704.
45. Z. Gu, F. Liu, E. A. Tonkova, S. Y. Lee, D. J. Tschumperlin, M. B. Brenner, Soft matrix is a natural stimulator for cellular invasiveness, *Mol. Biol. Cell*, **25** (2014), 457–469.
46. A. M. Hofer, S. Curci, M. A. Doble, E. M. Brown, D. I. Soybel, Intercellular communication mediated by the extracellular calcium-sensing receptor, *Nat. Cell Biol.*, **2** (2000), 392–398.
47. R. Shuttleworth, D. Trucu, Multiscale modelling of fibres dynamics and cell adhesion within moving boundary cancer invasion, *Bull. Math. Biol.*, **81** (2019), 2176–2219.
48. C. Guiot, P. Degiorgis, P. Delsanto, P. Gabriele, T. Diesboeck, Does tumour growth follow a “universal law”?, *J. Theor. Biol.*, **225** (2003), 147–151.
49. A. Laird, Dynamics of tumour growth, *Br. J. Cancer*, **18** (1964), 490–502.
50. D. Hanahan, R. A. Weinberg, Hallmarks of cancer: The next generation, *Cell*, **144** (2011), 646–674.
51. R. A. Weinberg, *The Biology of Cancer*, Garland Science, New York, 2006.
52. P. R. Halmos, *Measure Theory*, Springer-Verlag, New York, USA, 1974.
53. S. Suveges, R. Eftimie, D. Trucu, Directionality of macrophages movement in tumour invasion: A multiscale moving-boundary approach, *Bull. Math. Biol.*, **82** (2020), 1–48.
54. B. I. Camara, H. Mokrani, E. Afenya, Mathematical modeling of glioma therapy using oncolytic viruses, *Math. Biosci. Eng.*, **10** (2013), 565–578.
55. K. J. Painter, N. J. Armstrong, J. A. Sherratt, The impact of adhesion on cellular invasion processes in cancer and development, *J. Theor. Biol.*, **264** (2010), 1057–1067.
56. R. Shuttleworth, D. Trucu, Multiscale dynamics of a heterotypic cancer cell population within a fibrous extracellular matrix, *J. Theor. Biol.*, **486** (2020), 110040.
57. L. Peng, D. Trucu, P. Lin, A. Thompson, M. A. J. Chaplain, A multiscale mathematical model of tumour invasive growth, *Bull. Math. Biol.*, **79** (2017), 389–429.

58. T. Alzahrani, R. Eftimie, D. Trucu, Multiscale moving boundary modelling of cancer interactions with a fusogenic oncolytic virus: The impact of syncytia dynamics, *Math. Biosci.*, **323** (2020), 108296.

Appendix

A. Indicator functions enabling computations exclusively on the tumour moving domain

In order to carry out the macro-scale computation exclusively on the developing tumour $\Omega(t_0)$, for any $t_0 > 0$, we define the spatial cancer indicator function $\mathcal{I}(\cdot, \cdot) : \{1, \dots, M\} \times \{1, \dots, M\} \rightarrow \{0, 1\}$ given by

$$\mathcal{I}(s, p) := \begin{cases} 1 & \text{if } (x_s, x_p) \in \Omega(t_0), \\ 0 & \text{if } (x_s, x_p) \notin \Omega(t_0). \end{cases} \quad (\text{A.1})$$

Further, in order to identify the immediate outside nodes that are neighbours to the tumour boundary (which are needed during the computation), we define the spatially closest outside neighbour indicator functions $\mathcal{H}_{x,+1}(\cdot, \cdot), \mathcal{H}_{x,-1}(\cdot, \cdot), \mathcal{H}_{y,+1}(\cdot, \cdot), \mathcal{H}_{y,-1}(\cdot, \cdot) : \{2, \dots, M-1\} \times \{2, \dots, M-1\} \rightarrow \{0, 1\}$, defined by

$$\begin{aligned} \mathcal{H}_{x,\pm 1}(s, p) &:= |\mathcal{I}(s, p) - \mathcal{I}(s, p \pm 1)| \cdot \mathcal{I}(s, p), \\ \mathcal{H}_{y,\pm 1}(s, p) &:= |\mathcal{I}(s \pm 1, p) - \mathcal{I}(s, p)| \cdot \mathcal{I}(s, p). \end{aligned} \quad (\text{A.2})$$

These enable us to exercise the computations for the cancer cells dynamics only on the expanding cancer region $\Omega(t_0)$. Indeed, these indicator functions allow us to take advantage of the zero-flux conditions at the moving boundary $\partial\Omega(t_0)$ and appropriately assign density values that are required in computations (and that are dictated by the boundary conditions) at each of these closest outside points to the tumour boundary (along each spatial direction). Finally, these closest outside points to the tumour boundary are given by the union of pre-images $\mathcal{H}_{x,-1}^{-1}(\{1\}) \cup \mathcal{H}_{x,+1}^{-1}(\{1\}) \cup \mathcal{H}_{y,-1}^{-1}(\{1\}) \cup \mathcal{H}_{y,+1}^{-1}(\{1\})$.

B. Finite difference-midpoint involving indicator function

This section explain finite difference-midpoint method used through the paper, into two subsections local flux and non-local flux to accounts for all fluxes considered in this paper.

B.1. Non-local flux

At any spatial discretised spatial location $(x_s^1, x_p^2) \in \Omega(t_0)$, and any discretised time $t_l := t_0 + l\delta t$, $\forall l \in \{0, \dots, [\Delta t/\delta t]\}$, we denote by $c_{s,p}^l$ the discretised densities at the $((x_s^1, x_p^2), t_l)$ for each of the subpopulations $c \in \{c_p, i_p, c_m, i_m\}$. Similar notations we adopt also for the discretised adhesion fluxes at $((x_s^1, x_p^2), t_l)$, namely $\mathcal{A}_{c,s,p}^l$ stands for the discretised adhesion flux for each of the subpopulations $c \in \{c_p, i_p, c_m, i_m\}$. In this context, using the zero-flux conditions across the tumour's moving boundary (accounted here for via the indicators in equations Eqs (A.1) and (A.2)), we are able to carry out computations on the expanding spatial mesh by involving midpoint approximations for the cancer

subpopulation densities

$$\begin{aligned} c_{s,p\pm\frac{1}{2}}^l &:= \frac{c_{s,p}^l + [\mathcal{H}_{x,\pm 1}(s,p)c_{s,p}^l + \mathcal{I}(s,p\pm 1)c_{s,p\pm 1}^l]}{2}, \\ c_{s\pm\frac{1}{2},p}^l &:= \frac{c_{s,p}^l + [\mathcal{H}_{y,\pm 1}(s,p)c_{s,p}^l + \mathcal{I}(s\pm 1,p)c_{s\pm 1,p}^l]}{2}, \end{aligned} \quad (\text{B.1})$$

as well as for the adhesion fluxes

$$\begin{aligned} \mathcal{A}_{c,s,p\pm\frac{1}{2}}^l &:= \frac{\mathcal{A}_{c,s,p}^l + [\mathcal{H}_{x,\pm 1}(s,p)\mathcal{A}_{c,s,p}^l + \mathcal{I}(s,p\pm 1)\mathcal{A}_{c,s,p\pm 1}^l]}{2}, \\ \mathcal{A}_{c,s\pm\frac{1}{2},p}^l &:= \frac{\mathcal{A}_{c,s,p}^l + [\mathcal{H}_{y,\pm 1}(s,p)\mathcal{A}_{c,s,p}^l + \mathcal{I}(s\pm 1,p)\mathcal{A}_{c,s\pm 1,p}^l]}{2}, \end{aligned} \quad (\text{B.2})$$

while the central differences at the virtual midpoint nodes $(s, p \pm \frac{1}{2})$ and $(s \pm \frac{1}{2}, p)$ are given by:

for c :

$$\begin{aligned} [c_x]_{s,p+\frac{1}{2}}^l &:= \frac{[\mathcal{H}_{x,+1}(s,p)c_{s,p}^l + \mathcal{I}(s,p+1)c_{s,p+1}^l] - c_{s,p}^l}{\Delta x}, \\ [c_x]_{s,p-\frac{1}{2}}^l &:= \frac{c_{s,p}^l - [\mathcal{H}_{x,-1}(s,p)c_{s,p}^l + \mathcal{I}(s,p-1)c_{s,p-1}^l]}{\Delta x}, \\ [c_y]_{s+\frac{1}{2},p}^l &:= \frac{[\mathcal{H}_{y,+1}(s,p)c_{s,p}^l + \mathcal{I}(s+1,p)c_{s+1,p}^l] - c_{s,p}^l}{\Delta y}, \\ [c_y]_{s-\frac{1}{2},p}^l &:= \frac{c_{s,p}^l - [\mathcal{H}_{y,-1}(s,p)c_{s,p}^l + \mathcal{I}(s-1,p)c_{s-1,p}^l]}{\Delta y}, \end{aligned} \quad (\text{B.3})$$

Hence, the discretisation of the spatial operator $\nabla \cdot [D_c \nabla c - c \mathcal{A}_c(t, x, \mathbf{u}(t, \cdot))]$ in Eq (2.25c) is obtained by

$$\begin{aligned} (\nabla \cdot [D_c \nabla c - c \mathcal{A}_c(t, x, \mathbf{u}(t, \cdot))])_{s,p}^l &\approx \frac{D_c \left([c_x]_{s,p+\frac{1}{2}}^l - [c_x]_{s,p-\frac{1}{2}}^l \right) - c_{s,p+\frac{1}{2}}^l \cdot \mathcal{A}_{c,s,p+\frac{1}{2}}^l + c_{s,p-\frac{1}{2}}^l \cdot \mathcal{A}_{c,s,p-\frac{1}{2}}^l}{\Delta x} \\ &+ \frac{D_c \left([c_y]_{s+\frac{1}{2},p}^l - [c_y]_{s-\frac{1}{2},p}^l \right) - c_{s+\frac{1}{2},p}^l \cdot \mathcal{A}_{c,s+\frac{1}{2},p}^l + c_{s-\frac{1}{2},p}^l \cdot \mathcal{A}_{c,s-\frac{1}{2},p}^l}{\Delta y}. \end{aligned} \quad (\text{B.4})$$

Denoting now by $\mathcal{F}_{c,s,p}^l$ the discretised value of the flux $\mathcal{F}_c := D_c \nabla c - c \mathcal{A}_c(t, x, \mathbf{u}(t, \cdot))$ at the spatio-temporal node $((x_s, x_p), t_l)$, we observe that the discretisation of $\nabla \cdot \mathcal{F}_c = \nabla \cdot [D_c \nabla c - c \mathcal{A}_c(t, x, \mathbf{u}(t, \cdot))]$ given in Eq (2.25c) can therefore be equivalently expressed in a compact form as

$$(\nabla \cdot \mathcal{F}_c)_{s,p}^l \approx \frac{\mathcal{F}_{c,s,p+\frac{1}{2}}^l - \mathcal{F}_{c,s,p-\frac{1}{2}}^l + \mathcal{F}_{c,s+\frac{1}{2},p}^l + \mathcal{F}_{c,s-\frac{1}{2},p}^l}{h}, \quad (\text{B.5})$$

where

$$\begin{aligned} \mathcal{F}_{c,s,p\pm\frac{1}{2}}^l &= D_c [c_x]_{s,p\pm\frac{1}{2}}^l - c_{s,p\pm\frac{1}{2}}^l \cdot \mathcal{A}_{c,s,p\pm\frac{1}{2}}^l, \\ \mathcal{F}_{c,s\pm\frac{1}{2},p}^l &= D_c [c_y]_{s\pm\frac{1}{2},p}^l - c_{s\pm\frac{1}{2},p}^l \cdot \mathcal{A}_{c,s\pm\frac{1}{2},p}^l. \end{aligned}$$

B.2. Local flux

For the case when the spatial flux is given through the local operator $\mathcal{F}_c := D_c \Delta c - \eta_c \nabla \cdot c \nabla e$ where $c \in \{c_p, i_p, i_m\}$, we have the discretisation

$$(\mathcal{F}_c)_{s,p}^l \approx \frac{D_c \left([c_x]_{s,p+\frac{1}{2}}^l - [c_x]_{s,p-\frac{1}{2}}^l \right) - \eta_c c_{s,p+\frac{1}{2}}^l \cdot [e_x]_{s,p+\frac{1}{2}}^l + \eta_c c_{s,p-\frac{1}{2}}^l \cdot [e_x]_{s,p-\frac{1}{2}}^l}{\Delta x} + \frac{D_c \left([c_y]_{s+\frac{1}{2},p}^l - [c_y]_{s-\frac{1}{2},p}^l \right) - \eta_c c_{s+\frac{1}{2},p}^l \cdot [e_y]_{s+\frac{1}{2},p}^l + \eta_c c_{s-\frac{1}{2},p}^l \cdot [e_y]_{s-\frac{1}{2},p}^l}{\Delta y}, \quad (\text{B.6})$$

where

$$c_{s,p\pm\frac{1}{2}}^l := \frac{c_{s,p}^l + [\mathcal{H}_{x,\pm 1}(s,p)c_{s,p}^l + \mathcal{I}(s,p\pm 1)c_{s,p\pm 1}^l]}{2}, \quad (\text{B.7})$$

$$c_{s\pm\frac{1}{2},p}^l := \frac{c_{s,p}^l + [\mathcal{H}_{y,\pm 1}(s,p)c_{s,p}^l + \mathcal{I}(s\pm 1,p)c_{s\pm 1,p}^l]}{2},$$

and

$$[c_x]_{s,p+\frac{1}{2}}^l := \frac{[\mathcal{H}_{x,+1}(s,p)c_{s,p}^l + \mathcal{I}(s,p+1)c_{s,p+1}^l] - c_{s,p}^l}{\Delta x},$$

$$[c_x]_{s,p-\frac{1}{2}}^l := \frac{c_{s,p}^l - [\mathcal{H}_{x,-1}(s,p)c_{s,p}^l + \mathcal{I}(s,p-1)c_{s,p-1}^l]}{\Delta x}, \quad (\text{B.8})$$

$$[c_y]_{s+\frac{1}{2},p}^l := \frac{[\mathcal{H}_{y,+1}(s,p)c_{s,p}^l + \mathcal{I}(s+1,p)c_{s+1,p}^l] - c_{s,p}^l}{\Delta y},$$

$$[c_y]_{s-\frac{1}{2},p}^l := \frac{c_{s,p}^l - [\mathcal{H}_{y,-1}(s,p)c_{s,p}^l + \mathcal{I}(s-1,p)c_{s-1,p}^l]}{\Delta y},$$

and for e :

$$[e_x]_{s,p+\frac{1}{2}}^l := \frac{e_{s,p+1}^l - e_{s,p}^l}{h}, \quad \text{and} \quad [e_x]_{s,p-\frac{1}{2}}^l := \frac{e_{s,p}^l - e_{s,p-1}^l}{h}, \quad (\text{B.9})$$

$$[e_y]_{s+\frac{1}{2},p}^l := \frac{e_{s+1,p}^l - e_{s,p}^l}{h}, \quad \text{and} \quad [e_y]_{s-\frac{1}{2},p}^l := \frac{e_{s,p}^l - e_{s-1,p}^l}{h}.$$

Finally, for the haptotactic-like virus spatial operator $\eta_v \nabla \cdot (v \nabla e)$ is discretised as

$$(-\eta_v \nabla \cdot (v \nabla e))_{s,p}^l \approx \frac{-\eta_v v_{s,p+\frac{1}{2}}^l \cdot [e_x]_{s,p+\frac{1}{2}}^l + \eta_v v_{s,p-\frac{1}{2}}^l \cdot [e_x]_{s,p-\frac{1}{2}}^l}{\Delta x} + \frac{-\eta_v v_{s+\frac{1}{2},p}^l \cdot [e_y]_{s+\frac{1}{2},p}^l + \eta_v v_{s-\frac{1}{2},p}^l \cdot [e_y]_{s-\frac{1}{2},p}^l}{\Delta y}, \quad (\text{B.10})$$

C. The predictor-corrector

We denote by $H_c(\cdot, \cdot, \cdot)$ the right-hand side spatial operator for each of the tumour subpopulations Eq 2.25(a)–(d), with the non-transport part of this operator further denoted by $f_c(\mathbf{u}, v)$. Then, maintaining the same notation style, at any discretised spatio-temporal node $((x_s, x_p), t_l)$, we have that

$$H_c(\mathcal{F}_{c,s,p}^l, c_{s,p}^l, \mathbf{u}_{s,p}^l) := (\nabla \cdot \mathcal{F}_c)_{s,p}^l + f_c(\mathbf{u}_{s,p}^l, v_p^l). \quad (\text{C.1})$$

On the time interval $[t_l, t_{l+1}]$, we first predict c at $t_{l+\frac{1}{2}}$ using an explicit method as follows

$$\tilde{c}_{s,p}^{l+\frac{1}{2}} = c_{s,p}^l + \frac{\Delta t}{2} H_c(\mathcal{F}_{c,s,p}^l, c_{i,j}^l, \mathbf{u}_{s,p}^l). \quad (\text{C.2})$$

Further, using $\tilde{c}_{s,p}^{l+\frac{1}{2}}$ we calculate the corresponding predicted flux $\tilde{\mathcal{F}}_{c,s,p}^{l+\frac{1}{2}}$ at $t_{l+\frac{1}{2}}$. Then, we construct a non-local corrector that involves the average of the flux at the active neighbouring spatial locations

$$\{(x_s, x_{p\pm 1})\}, \{(x_{s\pm 1}, x_p)\}, \{(x_{s\pm 1}, x_{p-1})\}, \{(x_{s\pm 1}, x_{p+1})\} \cap \Omega(t_0). \quad (\text{C.3})$$

Denoting the set of indices corresponding to these active locations by \mathcal{N} , we establish a corrector for the spatial flux, given by

$$\mathcal{F}_{c,s,p}^{*l+\frac{1}{2}} = \frac{1}{\text{card}(\mathcal{N})} \sum_{(\sigma,\zeta) \in \mathcal{N}} \tilde{\mathcal{F}}_{c,\sigma,\zeta}^{l+\frac{1}{2}}, \quad (\text{C.4})$$

which ultimately enables us to use a trapezoidal-type approximation and obtain a corrected value for c at $t_{l+\frac{1}{2}}$ as

$$c_{s,p}^{l+\frac{1}{2}} = c_{s,p}^l + \frac{\Delta t}{4} \left[H_c(\mathcal{F}_{s,p}^l, c_{i,j}^l, \mathbf{u}_{s,p}^l) + H_c(\mathcal{F}_{s,p}^{*l+\frac{1}{2}}, \tilde{c}_{s,p}^{l+\frac{1}{2}}, \tilde{\mathbf{u}}_{s,p}^{l+\frac{1}{2}}) \right], \quad (\text{C.5})$$

Here, $\tilde{\mathbf{u}}_{s,p}^{l+\frac{1}{2}}$ is the "half-time predicted" tumour vector obtained for the current subpopulation c given by the half-time predicted value $\tilde{c}_{s,p}^{l+\frac{1}{2}}$, while all the other tumour subpopulations and the ECM (that enter as components of \mathbf{u}) being given by their accepted values at $((x_s, x_p), t_l)$.

Then, using

$$\bar{c}_{s,p}^{l+\frac{1}{2}} := \frac{c_{s,p}^{l+\frac{1}{2}} + c_{s,p}^l}{2}, \quad (\text{C.6})$$

to calculate the flux $\mathcal{F}_c^{l+\frac{1}{2}}$ at $t_{l+\frac{1}{2}}$, we initiate the predictor-corrector steps described above on the second half of this time interval, which we now repeat on $[t_{l+\frac{1}{2}}, t_{l+1}]$, and we finally obtain $c_{s,p}^{l+1}$ given through the analogue of Eq (C.5) that results (through the same procedure, described in Eqs (C.2)–(C.5)) on this second half-interval (i.e., on $[t_{l+\frac{1}{2}}, t_{l+1}]$). Finally, the same time-marching steps are adopted also for virus equations Eq (2.25f).



AIMS Press

©2021 the Author(s), licensee AIMS Press. This is an open access article distributed under the terms of the Creative Commons Attribution License (<http://creativecommons.org/licenses/by/4.0>)